GEOLOGY | THE GEOLOGICAL SOCIETY OF AMERICA®

https://doi.org/10.1130/G46563.1

Manuscript received 3 March 2019
Revised manuscript received 26 May 2019
Manuscript accepted 20 June 2019

Published online 10 July 2019

Curved slickenlines preserve direction of rupture propagation

Jesse Kearse[1,2], Yoshihiro Kaneko[1], Tim Little[2], and Russ Van Dissen[1]
[1]GNS Science, 1 Fairway Drive, Lower Hutt, New Zealand
[2]Victoria University of Wellington, Kelburn Parade, Wellington 6012, New Zealand

ABSTRACT

Slip-parallel grooves (striations) on fault surfaces are considered a robust indicator of fault slip direction, yet their potential for recording aspects of earthquake rupture dynamics has received little attention. During the 2016 Kaikōura earthquake (South Island, New Zealand), >10 m of dextral strike-slip on the steeply dipping Kekerengu fault exhumed >200 m^2 of fresh fault exposure (free faces) where it crossed bedrock canyons. Inscribed upon these surfaces, we observed individual striae up to 6 m long, all of which had formed during the earthquake. These were typically curved. Using simulations of spontaneous dynamic rupture on a vertical strike-slip fault, we reproduce the curved morphology of striae on the Kekerengu fault. Assuming strike-slip pre-stress, our models demonstrate that vertical tractions induced by slip in the so-called cohesive zone result in transient changes in slip direction. We show that slip-path convexity is sensitive to the direction of rupture propagation. To match the convexity of striae formed in 2016 requires the rupture to have propagated in a northeast direction, a prediction that matches the known rupture direction of the Kaikōura earthquake. Our study highlights the potential for fault striae to record aspects of rupture dynamics, including the rupture direction of paleo strike-slip earthquakes.

INTRODUCTION

The direction of earthquake rupture propagation exerts a profound influence on the distribution of strong ground shaking. As a consequence, damage and loss experienced by a community during an earthquake is dependent on the community's location relative to the direction of rupture propagation—a relationship especially true for large strike-slip events (Somerville et al., 1997; Gomberg et al., 2001). This effect has been observed in many large-magnitude strike-slip earthquakes in recent decades; e.g., the 1992 M_w 7.3 Landers (California) earthquake (Velasco et al., 1994), the 2002 M_w 7.9 Denali (Alaska) earthquake (Eberhart-Phillips et al., 2003), and the 2018 M_w 7.5 Palu (Indonesia) earthquake (Bao et al., 2019). Based on historical data, it is uncertain whether large-magnitude earthquakes systematically repeat their rupture direction; moreover, establishing the direction of past earthquakes using geological data has proved difficult. Previous studies have used structural data such as branching fault intersections (Poliakov et al., 2002; Fliss et al., 2005) and off-fault damage patterns in both ancient fault zones (Di Toro et al., 2005) and recent surface ruptures (Klinger et al., 2018) to infer rupture direction. However, these studies lack a context of seismological data with which to verify the rupture direction during a particular event.

Based on our literature review, out of ~55 surface ruptures observed geologically in the field since the late 1800s (Wesnousky, 2008; Biasi et al., 2013), 20 of the field datasets include measurements of coseismic slickenlines. Of these, 70% are curved, indicating that coseismic changes in slip direction are common (see the GSA Data Repository[1] and references therein). Spudich et al. (1998) used the curvature of slickenlines (up to 50°) found on the Nojima fault following the 1995 Kobe (Japan) earthquake to infer the magnitude of shear traction on the fault surface. However, aside from this pioneering work, the potential link between curved slickenlines and the dynamics of earthquake rupture has received little attention.

In this study, we propose that striae produced on fault plane surfaces during coseismic slip can reveal aspects of the dynamic rupture process. We present new slickenline data from fault surfaces that were exposed during the 2016 M_w 7.8 Kaikōura earthquake (South Island, New Zealand)—an event that has a well-established southwest-northeast rupture direction across ~200 km of the Pacific-Australian plate boundary in New Zealand (Hamling et al., 2017; Kaiser et al., 2017; Ando and Kaneko, 2018; Litchfield et al., 2018) (Fig. 1A). We observed curved coseismic striae on multiple fault outcrops along a 10 km section of the Kekerengu fault, the structure that yielded the greatest slip and moment release during this earthquake (Cesca et al., 2017; Holden et al., 2017). The systematic convexity of these striae records temporal changes in the coseismic slip direction on this fault. To uncover the mechanism that was responsible for the observed variation in slip direction, we undertook dynamic rupture modeling of a vertical strike-slip fault, using a simple set of boundary conditions. Here we discuss the potential for curved striae to record the rupture direction of paleo strike-slip earthquakes.

CURVED STRIAE ON THE KEKERENGU FAULT

The Kekerengu fault is part of the Marlborough Fault System, a series of mainly dextral faults that transfer slip between the Hikurangi megathrust and the Alpine fault (Fig. 1A). Dextral offset of Pleistocene terraces and uplift of the Seaward Kaikōura Ranges on its western side show that the Kekerengu fault is primarily strike-slip, with a lesser reverse component (Van Dissen et al., 2016). During the Kaikōura earthquake, many stream canyons were dextrally displaced 8–10 m and uplifted on their northwest sides by 1–2 m across the Kekerengu fault, which dips steeply to the northwest (>65° dip) (Kearse et al., 2018). Offset of these steep canyon walls (slopes of 20–30°) exhumed more than a dozen smooth

[1]GSA Data Repository item 2019306, table of historic surface-rupturing earthquakes; additional striae observations; near-fault geophysical data; model setup; snapshots of dynamic rupture; and alternative dynamic rupture models, is available online at http://www.geosociety.org/datarepository/2019/, or on request from editing@geosociety.org

CITATION: Kearse, J., Kaneko, Y., Little, T., and Van Dissen, R., 2019, Curved slickenlines preserve direction of rupture propagation: Geology, v. 47, p. 838–842, https://doi.org/10.1130/G46563.1

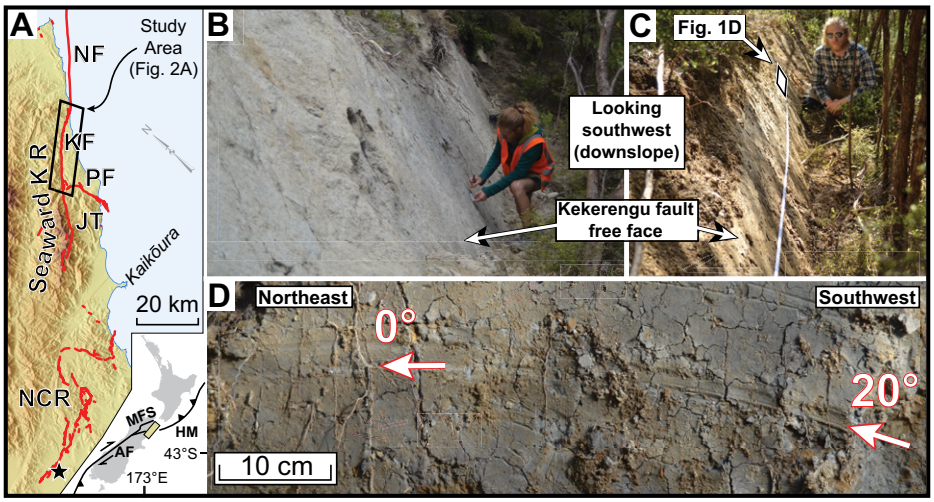

Figure 1. A: Map of surface ruptures in the 2016 Kaikōura earthquake (South Island, New Zealand) (bold red lines). KF—Kekerengu fault; NF—Needles fault; JT—Jordan thrust; PF—Papatea fault; NCR—North Canterbury Region; Seaward K R—Seaward Kaikōura Ranges. Inset shows the Pacific-Australian plate boundary, and location of the Marlborough Fault System (MFS), which separates the Hikurangi megathrust (HM) and the Alpine fault (AF). B,C: Examples of free face outcrops of the Kekerengu fault at site 3 (B; photograph taken 25 days after the earthquake) and site 4 (C; photograph taken 21 days after the earthquake). The apparently normal sense of throw is an artifact of large dextral slip which exhumes the footwall side of the fault. D: Gouge-covered free face of the Kekerengu fault at site 4, showing curved striation. Path of this 'convex-up' striation (right to left) describes initial dextral-reverse motion at a rake of 20°, which becomes pure strike slip (rake of 0°) as displacement accrues. Fault surface dips toward the viewer.

and near-planar fault surfaces (free faces; Figures 1B and 1C) that were ≤7 m long in the slip direction, each coated in a 1–2 cm layer of soft fault gouge (Fig. 1D). Nine of these free faces hosted coseismic fault striae that were curved (Fig. 2A). For example, Figure 1D depicts a striation where slip initiated as dextral-reverse motion, and as further displacement accrued, the direction of slip curved to become nearly pure strike-slip. This convex-up slip path was repeated at six out of the nine sites that contained curved striae, with some sites containing many measurement locations where striae were recorded (Fig. 2A; see the Data Repository). Curved striae were found mostly on the upper part of the free face, suggesting they were formed early in the rupture. The angular magnitude of the observed convexity is typically ~15° and is >40° at sites 3 and 7. At two sharp bends in the fault trace, the sense of uplift was opposite to the dominant one, and their striae describe a convex-down slip path (sites 1, 7, and 9; Fig. 2A). In all cases, the incremental magnitude of fault slip—both vertical and dextral—recorded by the individual fault striae segments (0.2–6 m) amounts to only a fraction of the known coseismic net displacement at these sites, which was 8–10 m. Post-earthquake erosion of free faces in the days to months following the earthquake undoubtedly curtailed the length of individual straie; however, some striae become increasingly diffuse toward their 'downstream' ends (Fig. 1D), suggesting a different process is responsible for their limited length. Near-fault geodetic and seismological data collected at two stations (the KEKS seismic station, and a high-rate continuous GPS station located 30 km northeast of the study area) on the northwest side of the Kekerengu fault during the earthquake (Fig. 2A; see the Data Repository) imply that the initial ~5 s of rupturing on the Kekerengu fault accumulated up to 4 m of almost pure dextral-slip and <0.3 m of throw, whereas most of the throw (1–2 m) began accumulating 4–7 s after this. The available geological and geophysical data sug-

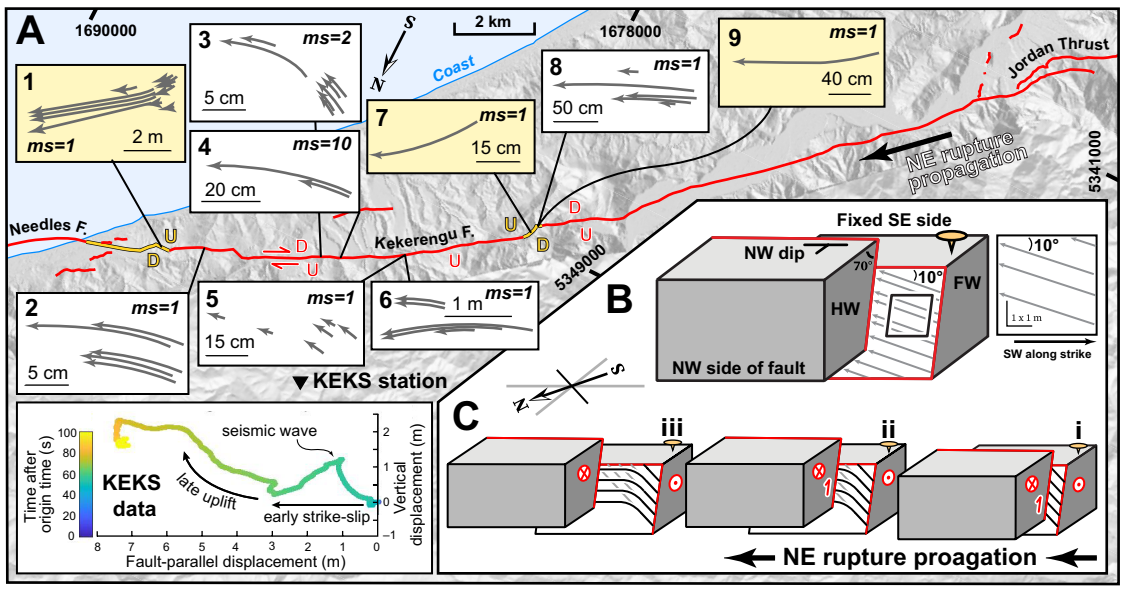

Figure 2. A: Kekerengu fault (South Island, New Zealand) surface rupture map and catalog of curved striae that formed in the 2016 Kaikōura earthquake. Each box represents a fault-plane view of the Kekerengu fault, with site numbers in the upper left-hand corner, and number of specific measurement locations at a particular site indicated (e.g., ms = 10). Sites 1, 7, and 9 show the opposite sense of curvature, and are located at sharp bends in the fault, which also show southeast-up displacements. Inset shows displacement time history at seismic station KEKS (located 2.7 km from the Kekerengu fault). Up (U) and down (D) refer to the relative sense of throw on the Kekerengu fault during the Kaikōura earthquake. Red sections of the rupture trace have northwest-up throw, gold sections have southeast-up throw. B: Block diagram showing the context for each site in A. Reference frame for A–C is relative to a fixed southeast side of the fault, and tracks the motion of the northwest side of the Kekerengu fault during the earthquake. C: Block diagram showing the sequence of fault slip on the Kekerengu fault during the Kaikōura earthquake, inferred from the curved striae. i—initial dextral-reverse motion; ii—transition toward strike-slip; iii—strike-slip motion. Gray striae on the fault surface were produced during period i, and were later overprinted by fault motion during periods ii and iii. Circle with dot represents relative block motion toward the southwest; circle with cross represents relative block motion toward the northeast.

gest that the curved striae on the Kekerengu fault were inscribed during the early phase of strike-slip–dominated rupturing (Fig. 2A).

DYNAMIC RUPTURE MODEL

To evaluate possible mechanisms for the curvature of Kekerengu fault striae, we simulated the spontaneous, dynamic rupture of a 50-km-long and 25-km-deep vertical strike-slip fault in layered elastic half space, using a spectral-element code (Ampuero, 2002; Kaneko et al., 2008). A horizontal initial shear traction was applied to the fault surface, with a magnitude that increased linearly with depth. Dynamic rupture was initiated by overstressing a small 3-km-wide patch in the center of the fault at a depth of 12 km, and then the rupture propagated spontaneously across the fault surface, where it was governed by slip-weakening friction laws (for additional details of the model setup, see the Data Repository).

Slip paths for 42 nodes on the fault surface (gray arrows in Fig. 3C) depict cseismic motion of the near-side of the fault relative to the far side. Their lengths depict slip magnitudes, and their shape and curvature illustrates any changes in slip direction. At depths >3 km, slip paths are horizontal and show little change in slip direction with time. For nodes located along mixed-mode rupture directions (Andrews, 1994) at depths <3 km, slip paths are more complex. At depths <3 km, slip follows a curved path during the initial few decimeters; at locations between x = 0 and x = –20 km (left side of Fig. 3C), curvature is convex-up (Fig. 3A), while on the other side of the hypocenter between x = 0 and x = 20 km (right side of Fig. 3C), curvature is convex-down (Fig. 3B). As further displacement is accrued, slip directions converge toward a horizontal rake of 180°. These results do not necessarily imply that one side of the fault experiences an opposing sense of net uplift at either end of a rupture (this is only true for cases with pure strike-slip pre-stress). Rather, our results suggest that the convexity of the initial slip path is opposite at either end of the rupture, regardless of the rake of initial shear traction on the fault (see the Data Repository).

MECHANISM FOR CHANGES IN SLIP DIRECTION

The mechanism behind transient changes in slip direction in our dynamic model is consistent with the one proposed by Spudich et al. (1998). Dynamic changes in rake angle are driven by vertical stress changes along mixed-mode rupture directions produced within the so-called cohesive zone (the part of the fault that is slipping but has not yet fully weakened). Seismic waves are continuously generated within this zone, and they carry vertical stresses that induce vertical components of slip on the sliding surface. At depths below 3 km, confining stresses are large compared to the dynamic loads, a relationship that suppresses the magnitude of these transient vertical motions. Yet slip at these depths retains subtle (<2°) temporal changes in slip direction, and exhibits the same reversal in path convexity on either side of the hypocenter (left versus right sides of Figure 3C are yellow and green, respectively; see the Data Repository). Near Earth's surface, where confining stresses are low, the ratio of dynamic to confining stress is larger, promoting a larger magnitude of coseismic vertical slip. As the rupture front propagates along strike, the model predicts opposite senses of slip deflection near the two propagating rupture tips: convex-upward on one side and convex-downward on the other. Figure 4 details changes in shear traction and slip velocity at the rupture tip to highlight the correlation between vertical stress and rotation of the slip direction.

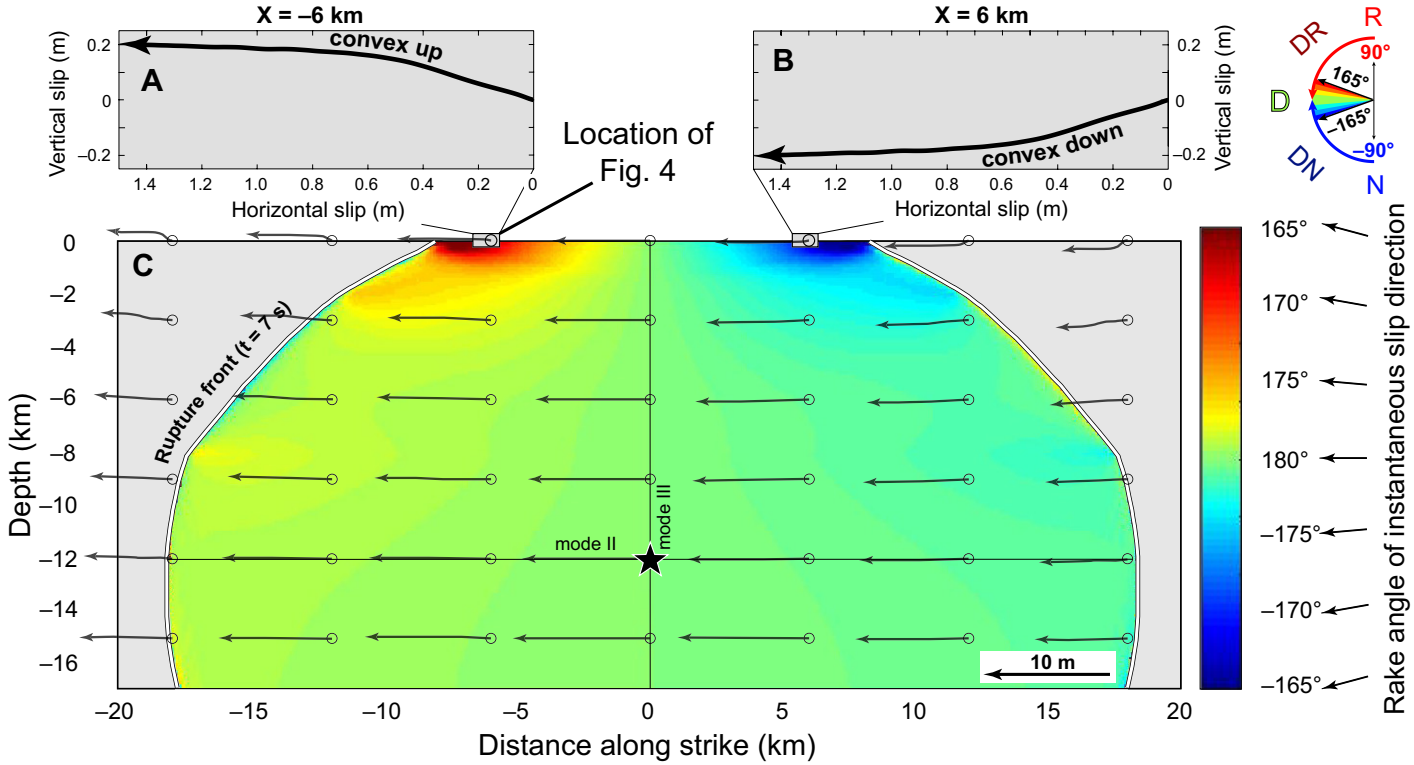

Figure 3. Fault-pane view of dynamic rupture simulation results. Colors and slip paths (arrows) describe the motion of the near side of the fault relative to the far side. A: Initial slip paths for the node at distance *x* = –6 km and depth *z* = 0 km. Note that the convex-up nature of slip paths at nodes to the left (northeast) of the hypocenter are consistent with on-fault observations on the Kekerengu fault following the Kaikōura earthquake (South Island, New Zealand). B: Initial slip path for the node at *x* = 6 km and *z* = 0 km. C: Colormap corresponds to a snapshot of dynamic rupture 7 s after rupture nucleation. At this stage, localized patches of steep rake angle have developed within the top 3 km in the immediate wake of the rupture front. As the rupture progresses, these areas of inclined slip direction (red and blue patches) track the rupture front as it propagates bilaterally away from the hypocenter (detailed maps of rupture evolution are available in the Data Repository [see footnote 1]). Rake angles >2° (red and blue colors) are only produced near the surface. Star indicates the site of rupture nucleation. R—reverse; N—normal; D—dextral; DR—dextral-reverse; DN—dextral-normal.

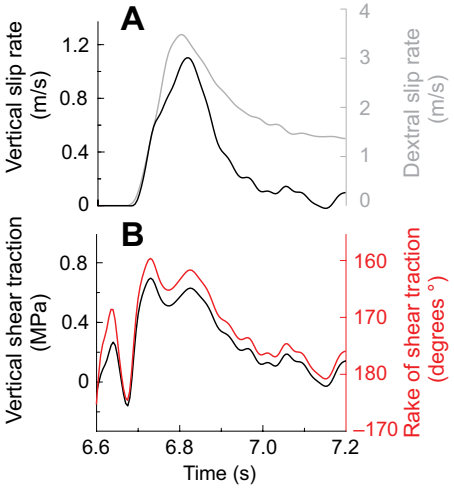

Figure 4. Details of on-fault slip and shear traction as the rupture front arrives at the node at distance *x* = –6 km and depth *z* = 0 km (see Fig. 3). A: Vertical (black) and dextral (gray) slip rate. B: Vertical shear traction (black) and rake angle of shear traction (red). Fault sliding accelerates from 0 m/s to a peak slip velocity of 3.6 m/s. This initial slip is accompanied by a rise in vertical shear stress from 0 MPa to 0.6 MPa, which induces vertical slip that peaks at ~1.1 m/s, resulting in 0.25 m of net slip at a rake of 165°. Over the following 0.2 s, as a further 0.5 m of slip is accrued, vertical shear stress relaxes to <0.1 MPa, and vertical slip rate decays to just 4% of the net slip rate of 1.7 m/s. It is this relaxation of the vertical shear traction (and thus vertical slip) that results in a rotation of the rake of slip from 165° to 180° (thus curving the slip path). Horizontal slip rate soon stabilizes at ~1.2 m/s and continues for ~7 s before rupture termination, culminating in 9.1 m of net slip. The initial part of this dynamic process is illustrated as the along-strike gradient of instantaneous slip direction (color-coding in Fig. 3C) between the rupture tip at *x* = ±17 km, *z* = 0 km, and *x* = 0 km.

DISCUSSION AND CONCLUSIONS

We note a correlation between the convexity of curved striae on the Kekerengu fault and results of our dynamic rupture model. As slip initiates, movement of the downstream side of the fault (the side moving in the direction of rupture propagation) follows a convex-up slip path that initially has a rake of ~15° to (and ultimately becomes parallel with) the direction of initial shear stress on the fault (Fig. 3A). Although several of our sites—specifically those at sharp fault bends—showed the opposite sense of slip-path convexity, we suggest that the kinematic differences at these areas induced local stresses that overwhelmed the more general dynamic effects described by our model. We therefore interpret the predominant pattern of slip-path curvature on the Kekerengu fault to have resulted from vertical stress changes in the cohesive zone of the northeast-propagating rupture of the Kaikōura earthquake. In addition, the curvature of striae seen on multiple exposures of the Nojima fault following the 1995 M_w 7.2 Kobe (Japan) earthquake (Otsuki et al., 1997) is consistent with our model, and with the known direction of rupture propagation in this event (Yoshida et al., 1996). These dynamic effects are likely not to be restricted to strike-slip faults, as mixed-mode dynamic rupture on dip-slip faults should also produce transient changes in initial slip direction, which may explain curved striae seen after events such as the 1954 M 7.0 Fairview Peak (Nevada, USA) (Slemmons, 1957) and 2011 M_w 6.6 Fukushima (Japan) earthquakes (Otsubo et al., 2013).

We offer two possible explanations for why striae on the Kekerengu fault capture only an early and small (typically <10% of total) increment of the 2016 slip. One possibility is that, at the onset of slip, the fault plane (in the near surface) was rough compared to the final stages of slip, having only just broken any cohesion gained during the interseismic period. If so, this might promote asperity ploughing and striae production at that early stage (Tesei et al., 2017), thus promoting a temporal bias in the striation record. According to this scenario, the early-formed asperities (i.e., topography in the new fracture surface) were progressively abraded during the accumulating slip, resulting in a smoother fault plane and a termination in striation production. Another possibility (and one that is not mutually exclusive with the former) is that during slip in the near-surface, along-strike translation of large (meter-scale) corrugations in the fault surface (e.g., Candela et al., 2012) promoted transient separation of the fault walls, thereby terminating the engraving process. Both ideas are supported by individual striae that are deeply inset near their inception point but are shallower and more diffuse toward their termination (e.g., Fig. 1D).

Spudich et al. (1998) together with Guatteri and Spudich (1998)—both of which assume depth-independent pre-stress—suggest that the fractional stress drop, defined as the ratio of the stress drop to the magnitude of initial shear stress, is ~0.7 on faults that exhibit large (>30°) changes in coseismic slip direction. In our model that features depth-dependent stress, in order to reproduce up to ~20° changes in slip direction on the Kekerengu fault, the fractional stress drop is ~0.2, which corresponds to the 'high stress' case of Guatteri and Spudich (1998). Even in the case of 'low stress', the pattern of slip-path convexity should still depend on rupture direction.

Striated fault surfaces are routinely measured in neotectonic and paleoseismic studies, including on well-preserved Holocene scarps and on excavated fault surfaces in paleoseismic trenches. Crosscutting or overlapping striae seen in such places do not necessarily represent the superposition of multiple earthquakes; and our results provide a simple explanation for transient changes in slip direction during a single slip episode, which can create overlapping striae (e.g., the 2011 Fukushima earthquake; Otsubo et al., 2013). More importantly, our study demonstrates that it may be possible to infer the rupture direction of paleoearthquakes in cases where coseismic striae record temporal changes in slip direction. To do this, we propose that data be collected from structurally simple parts of the fault that are representative of its overall kinematics, and that are also likely to generate and preserve striae. We further suggest that multiple sites be evaluated to establish any systematic patterns in striation convexity.

Temporal changes in slip direction during dynamic rupture are likely to be a widespread characteristic in the near-surface during large-magnitude earthquakes. Geological evidence of this type, when combined with simulations of dynamic rupture, may yield important insight into the near-field dynamics of fault slip, including the rupture direction of paleo strike-slip earthquakes and, by inference, the rupture direction of future strike-slip earthquakes; thereby helping to better constrain the distribution of damaging ground shaking in those events.

ACKNOWLEDGMENTS

Assistance in the field was provided by Sam Taylor-Offord and Alec Yates. This work was supported by Victoria University of Wellington (New Zealand) and a Rutherford Discovery Fellowship (Royal Society of New Zealand).

REFERENCES CITED

Ampuero, J.P., 2002, Etude physique et numérique de la nucléation des séismes [Ph.D. thesis]: Paris, University of Paris VII, 227 p.

Ando, R., and Kaneko, Y., 2018, Dynamic rupture simulation reproduces spontaneous multifault rupture and arrest during the 2016 M_w 7.9 Kaikoura earthquake: Geophysical Research Letters, v. 45, p. 12,875–12,883, https://doi.org/10.1029/2018GL080550.

Andrews, D.J., 1994, Dynamic growth of mixed-mode shear cracks: Bulletin of the Seismological Society of America, v. 84, p. 1184–1198.

Bao, H., Ampuero, J.P., Meng, L., Fielding, E.J., Liang, C., Feng, T., and Huang, H., 2019, Early and persistent supershear rupture of the 2018 M_w 7.5 Palu earthquake: Nature Geoscience, v. 12, p. 200–205, https://doi.org/10.1038/s41561-018-0297-z.

Biasi, G., Weldon, R. J., and Dawson, T. E., 2013, Distribution of slip in ruptures: Appendix F of Uniform California Earthquake Rupture Forecast Version 3 (UCERF3): U.S. Geological Survey Open File Report 2013-1165, https://pubs.usgs.gov/of/2013/1165/pdf/ofr2013-1165_appendixF.pdf.

Candela, T., Renard, F., Klinger, Y., Mair, K., Schmittbuhl, J., and Brodsky, E.E., 2012, Roughness of fault surfaces over nine decades of length scales: Journal of Geophysical Research: Solid Earth, v. 117, B08409, https://doi.org/10.1029/2011JB009041.

Cesca, S., Zhang, Y., Mouslopoulou, V., Wang, R., Saul, J., Savage, M., Heimann, S., Kufner, S.K., Oncken, O., and Dahm, T., 2017, Complex rupture process of the M_w 7.8, 2016, Kaikoura earthquake, New Zealand, and its aftershock sequence: Earth and Planetary Science Letters,

v. 478, p. 110–120, https://doi.org/10.1016/j.epsl.2017.08.024.
Di Toro, G., Nielsen, S., and Pennacchioni, G., 2005, Earthquake rupture dynamics frozen in exhumed ancient faults: Nature, v. 436, https://doi.org/10.1038/nature03910.
Eberhart-Phillips, D., et al., 2003, The 2002 Denali fault earthquake, Alaska: A large magnitude, slip-partitioned event: Science, v. 300, p. 1113–1118, https://doi.org/10.1126/science.1082703, https://doi.org/10.1126/science.1082703.
Fliss, S., Bhat, H.S., Dmowska, R., and Rice, J.R., 2005, Fault branching and rupture directivity: Journal of Geophysical Research: Solid Earth, v. 110, B06312, https://doi.org/10.1029/2004JB003368.
Gomberg, J., Reasenberg, P.A., Bodin, P.L., and Harris, R.A., 2001, Earthquake triggering by seismic waves following the Landers and Hector Mine earthquakes: Nature, v. 411, p. 462, https://doi.org/10.1038/35078053.
Guatteri, M., and Spudich, P., 1998, Coseismic temporal changes of slip direction: the effect of absolute stress on dynamic rupture: Bulletin of the Seismological Society of America, v. 88, p. 777–789.
Hamling, I.J., et al., 2017, Complex multifault rupture during the 2016 M_w 7.8 Kaikōura earthquake, New Zealand: Science, v. 356, https://doi.org/10.1126/science.aam7194.
Holden, C., Kaneko, Y., D'Anastasio, E., Benites, R., Fry, B., and Hamling, I.J., 2017, The 2016 Kaikōura earthquake revealed by kinematic source inversion and seismic wavefield simulations: Slow rupture propagation on a geometrically complex crustal fault network: Geophysical Research Letters, v. 44, p. 11,320–11,328, https://doi.org/10.1002/2017GL075301.
Kaiser, A., et al., 2017, The 2016 Kaikōura, New Zealand, earthquake: Preliminary seismological report: Seismological Research Letters, v. 88, p. 727–739, https://doi.org/10.1785/0220170018.
Kaneko, Y., Lapusta, N., and Ampuero, J.P., 2008, Spectral element modeling of spontaneous earthquake rupture on rate and state faults: Effect of velocity-strengthening friction at shallow depths: Journal of Geophysical Research: Solid Earth, v. 113, B09317, https://doi.org/10.1029/2007JB005553.
Kearse, J., et al., 2018, Onshore to offshore ground-surface and seabed rupture of the Jordan-Kekerengu-Needles fault network during the 2016 M_w 7.8 Kaikōura earthquake, New Zealand: Bulletin of the Seismological Society of America, v. 108, p. 1573–1595, https://doi.org/10.1785/0120170304.
Klinger, Y., et al., 2018, Earthquake damage patterns resolve complex rupture processes: Geophysical Research Letters, v. 45, p. 10,279–10,287, https://doi.org/10.1029/2018GL078842.
Litchfield, N.J., et al., 2018, Surface rupture of multiple crustal faults in the 2016 M_w 7.8 Kaikōura, New Zealand, earthquake: Bulletin of the Seismological Society of America, v. 108, p. 1496–1520, https://doi.org/10.1785/0120170300.
Otsubo, M., Shigematsu, N., Imanishi, K., Ando, R., Takahashi, M., and Azuma, T., 2013, Temporal slip change based on curved slickenlines on fault scarps along Itozawa fault caused by 2011 Iwaki earthquake, northeast Japan: Tectonophysics, v. 608, p. 970–979, https://doi.org/10.1016/j.tecto.2013.07.022.
Otsuki, K., Minagawa, J., Aono, M., and Ohtake, M., 1997, On the curved striations of Nojima seismic fault engraved at the 1995 Hyogoken-Nambu earthquake, Japan: Journal of the Seismological Society of Japan, v. 49, p. 451–460.
Poliakov, A.N.B., Dmowska, R., and Rice, J.R., 2002, Dynamic shear rupture interactions with fault bends and off-axis secondary faulting: Journal of Geophysical Research: Solid Earth, v. 107, B11, p. 2295, https://doi.org/10.1029/2001JB000572.
Slemmons, D.B., 1957, Geological effects of the Dixie valley–Fairview peak, Nevada, earthquakes of December 16, 1954: Bulletin of the Seismological Society of America, v. 47, no. 4, p. 353–375.
Somerville, P.G., Smith, N.F., Graves, R.W., and Abrahamson, N.A., 1997, Modification of empirical strong ground motion attenuation relations to include the amplitude and duration effects of rupture directivity: Seismological Research Letters, v. 68, no. 1, p. 199–222, https://doi.org/10.1785/gssrl.68.1.199.
Spudich, P., Guatteri, M., Otsuki, K., and Minagawa, J., 1998, Use of fault striations and dislocation models to infer tectonic shear stress during the 1995 Hyogo-ken Nanbu (Kobe) earthquake: Bulletin of the Seismological Society of America, v. 88, no. 2, p. 413–427.
Tesei, T., Carpenter, B.M., Giorgetti, C., Scuderi, M.M., Sagy, A., Scarlato, P., and Collettini, C., 2017, Friction and scale-dependent deformation processes of large experimental carbonate faults: Journal of Structural Geology, v. 100, p. 12–23, https://doi.org/10.1016/j.jsg.2017.05.008.
Van Dissen, R.J., et al., 2016, Late Quaternary dextral slip rate of the Kekerengu fault: New Zealand's third fastest on-land fault: New Zealand GeoSciences Society Conference, Wanaka, New Zealand, GeoSciences Society of New Zealand, Miscellaneous Publication 142A, 89 p.
Velasco, A.A., Ammon, C.J., and Lay, T., 1994, Empirical green function deconvolution of broadband surface waves: Rupture directivity of the 1992 Landers, California (M_w = 7.3), earthquake: Bulletin of the Seismological Society of America, v. 84, no. 3, p. 735–750.
Wesnousky, S.G., 2008, Displacement and geometrical characteristics of earthquake surface ruptures: Issues and implications for seismic-hazard analysis and the process of earthquake rupture: Bulletin of the Seismological Society of America, v. 98, no. 4, p. 1609–1632, https://doi.org/10.1785/0120070111.
Yoshida, S., Koketsu, K., Shibazaki, B., Sagiya, T., Kato, T., and Yoshida, Y., 1996, Joint inversion of near-and far-field waveforms and geodetic data for the rupture process of the 1995 Kobe earthquake: Journal of Physics of the Earth, v. 44, p. 437–454, https://doi.org/10.4294/jpe1952.44.437.

Printed in USA

GSA Data Repository 2019306

Kearse, J., Kaneko, Y., Little, T., and Van Dissen, R., 2019, Curved slickenlines preserve direction of rupture propagation: Geology, https://doi.org/10.1130/G46563.1

SUPPLEMENTARY MATERIAL A – TABLE OF HISTORIC SURFACE RUPTURING EARTHQUAKES.

Table S1 lists all the historic earthquakes that ruptured the ground surface, and which also have documented co-seismic striae that were observed in the field. The data are available within the articles listed next to each event.

Earthquake	*Magnitude*	*Mechanism*	*Max slip (m)*	*Fault Striae*	*Reference*
1915 Pleasant Valley, NV, U.S.	M_w 6.8	N	8.2	Linear	Jones (1915).
1937 Thuosou Lake, Tibet	M 7.5	SS-L	5.2	Linear	Guo, et al. (2007).
1954, Fairview Peaks, NV, U.S.	M_w^G 7.0	N SS-R	5.2	Curved	Slemmons (1957).
1957, Gobi-Altai, Mongolia.	M_w 8.1	SS-L	7	Curved	Florensov & Solonenko (1965).
1959, Hegben Lake, MT, U.S.	M 7.1	N	5.4	Linear	Witkind et al. (1962).
1969, Paiahuancha, Peru.	M 6.2	R	1.8	Curved	Philip & Megard (1977).
1974, Izu-Hanto-Oki, Japan.	M 6.9	SS-R	1	Curved	Kakimi et al. (1977).
1980, El Asnam, Algeria.	M_w 7.1	R	6.5	Curved	Philip & Meghraoui (1983).
1983, Borah Peak, ID, U.S.	M 7.0	N	4	Linear	Crone et al. (1987).
1988 Tennant Creek, Australia.	Ms 6.7	R	2.5	N/A	Crone et al. (1992).
1988 Spitak (Armenia), Armenia.	Ms 7.0	R	2.2	Curved	Avagyan et al. (2003).

1992, Landers, CA, U.S.	M_w 7.3	SS-R	6.7	Curved	Arrowsmith & Rhoades (1994).
1995, Neftegorsk, Russia.	Ms 7.6	SS-R	8.1	Curved (inferred)	Shimamoto et al., (1996).
1995, Hyogo-Ken Nanbu (Kobe), Japan.	M 7.2	SS-R	2.5	Curved	Otsuki et al. (1997).
1999 Hector Mine, CA, U.S.	M_w 7.1	SS-R	5.2	Linear	Treiman et al. (2002).
1999 Chi-Chi.	M_w 7.6	R SS-R	16.4	Linear	Lee et al. (2002).
2001, Kunlun (Kokoxili), Tibet.	M_w 7.8	SS-L	16.3	Linear (Supershear)	Lin et al. (2002).
2002, Denali, Alaska.	M_w 7.9	SS-R	8.8	Curved + Linear (Supershear)	Haeussler et al. (2004).
2008, Wenchuan, China.	M_w 8.0	R	6.5	Curved	Pan et al. (2014).
2010, El Mayor-Cucapah, Mexico	M_w 7.2	SS-R	3.9	Curved	Fletcher et al. (2014).
2011, Iwaki, Japan.	M_w 6.6	N	2.0	Curved	Otsubo et al. (2013).
2016, Kaikoura, New Zealand.	M_w 7.8	SS-R	11.9	Curved	Kearse et al. (2018).

Table S1: list of historic earthquakes for which there are documented co-seismic striae.

Of the total 22 earthquakes for which fault striae are noted, 13 show curved striae, 1 shows a disparity between net slip direction and striae – indicating temporal rake rotation (14 curved total), 7 are linear, and 1 does not specify whether recorded striations are linear or curved.

SUPPLEMENTAL MATERIAL B – ADDITIONAL STRIAE OBSERVATIONS

At sites 3 and 4 (Fig. 2A), there were multiple locations where we observed curved striae. These locations were spaced over a horizontal distance of ≤100 m (Fig. S1).

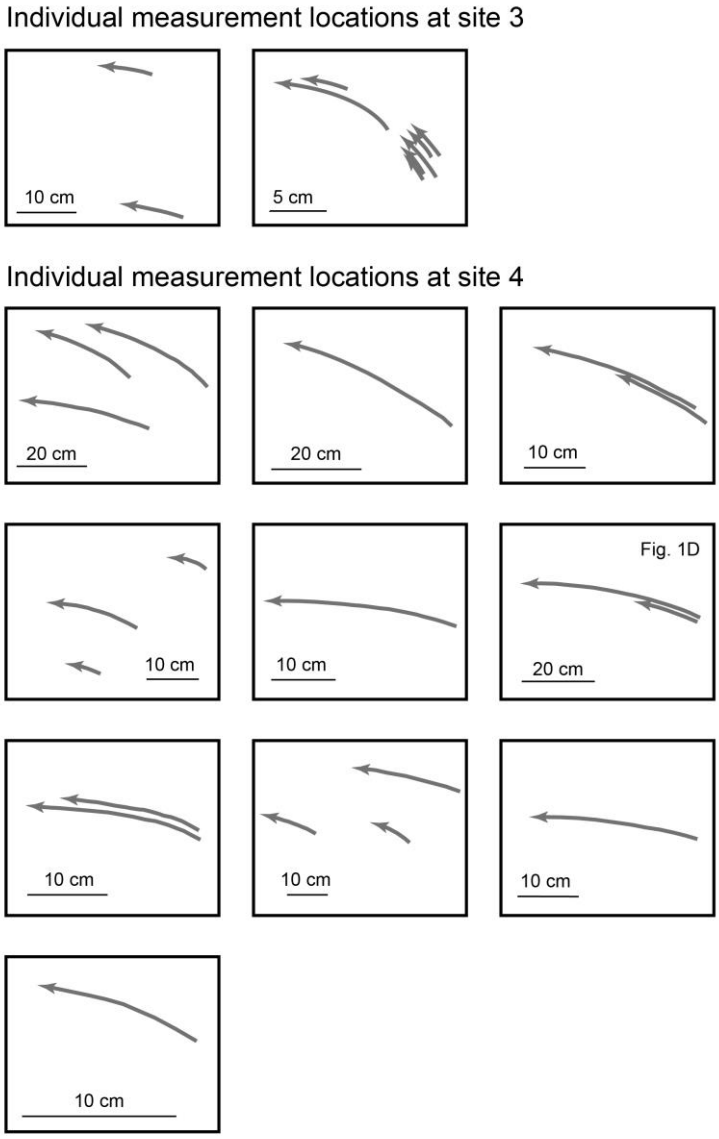

Figure S1. Fault-plane view of additional striae at sites 3 and 4 (see Fig. 2 for context).

SUPPLEMENTARY MATERIAL C – NEAR-FAULT GEOPHYSICAL DATA

To investigate the temporal evolution of fault displacement during rupture of the Kekerengu fault, we analyse near-fault instruments that record data at a high temporal resolution during the Kaikoura earthquake. We found two reliable instruments; one strong-motion seismograph (KEKS), located 2.7 km from where the curved striae were observed, on the hangingwall of the Kekerengu fault, and one high-rate (10 Hz) continuous GPS station located on the hangingwall of the Needles fault (Fig. S2).

Both instruments show initial strike-slip displacement followed 4–7 s after by ~1–2 m of hangingwall uplift. At KEKS, the first strong signal begins ~54 s after the origin time of the earthquake. Between 54–62 s this initial displacement is characterised by 3 m of fault-parallel displacement, with a transient component of vertical displacement that peaks at ~1.2 m and decays to ~0.2 m. We attribute this transient component of vertical displacement to passing seismic waves that were transmitted from the Kekerengu fault as it began to slip. Later in the rupture sequence, and beginning at ~66 s, KEKS starts to record an uplift signal of 1–2 m, which is comparable to the net uplift observed at the fault trace of the Kekerengu fault. At CMBL, the data are similar. Beginning at ~70 s, CMBL records 2 m fault-parallel displacement with <0.1 m of uplift. Later, at ~77 s, uplift of begins to accumulate, resulting in ~0.7 m of permanent vertical displacement.

Although CMBL is located on the hangingwall of the Needles fault, it is considered to be an extension of the Kekerengu fault (essentially the same fault, but with a different name). The coherent displacement signal (both strike-slip and uplift) seen along the hanginwall of both faults (e.g. in Hamling et al. 2017) suggests that they behaved as a single structure and accommodated a similar style of displacement during the Kaikoura earthquake.

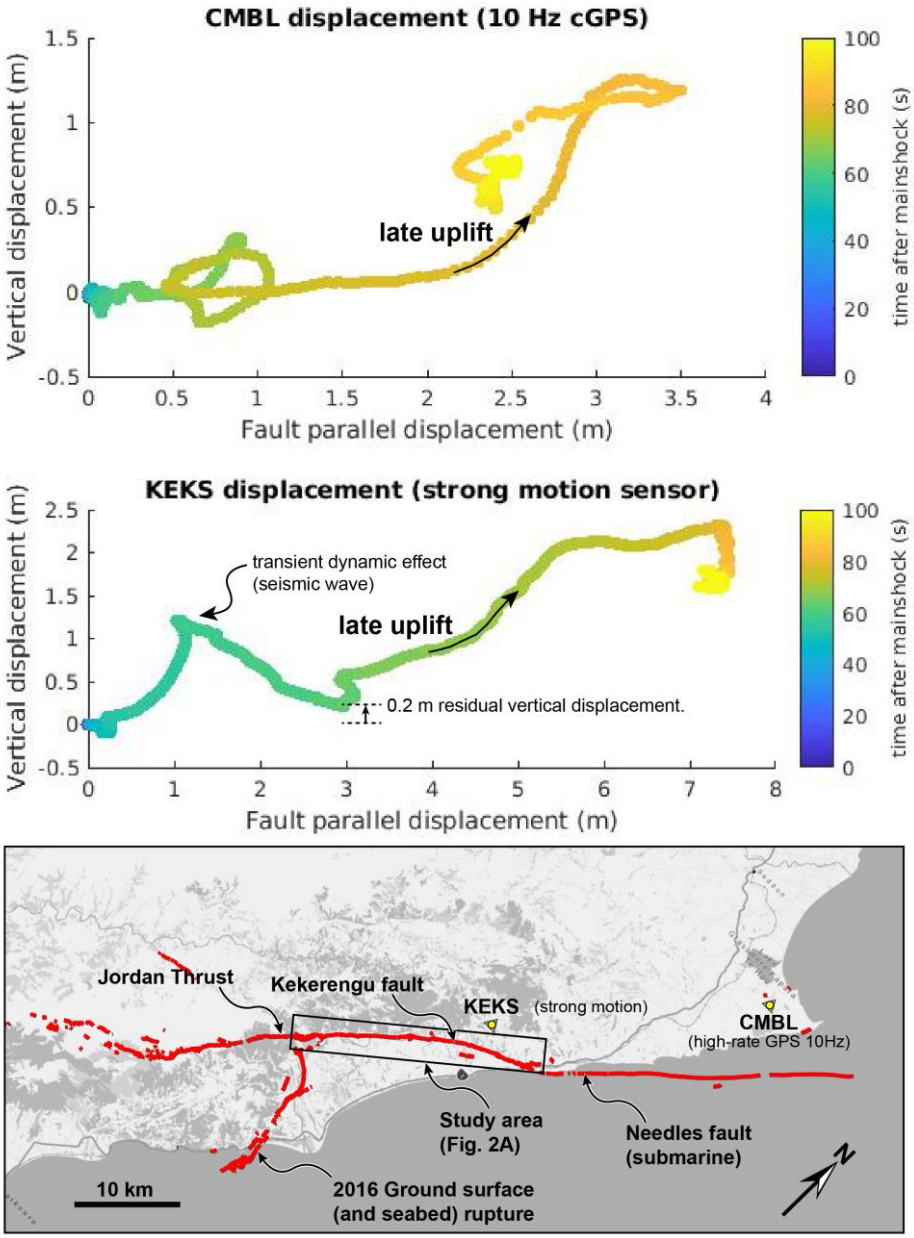

Figure S2. Near-fault geodetic and seismological data. Data from both stations have been processed into fault-parallel components of displacement: for details on processing of KEKS data see Kaneko et al. (2017), for details on the processing of CMBL data see Holden et al. (2017).

SUPPLEMENTARY MATERIAL D – MODEL SETUP

We simulate dynamic rupture scenarios on a 50 km by 25 km, right-lateral, vertical strike-slip fault embedded into a layered, elastic half-space (Figure S3; Table S2). While the actual Kekerengu fault dips steeply at 70 – 80 degrees to the northwest and may be listric at depth (Hamling et al., 2017; Xu et al., 2018), we assume a vertical strike-slip fault for both simplicity and generality. The constitutive response of the fault is governed by a linear slip-weakening friction law (Ida, 1972; Palmer and Rice, 1973), in which the shear strength of the fault linearly decreases from its static value τ_s to the dynamic value τ_d over a characteristic slip distance *Dc*. As in Bizzarri and Cocco (2003), we assume that the slip velocity vector is collinear with the shear traction vector at each instant in time at all fault node points.

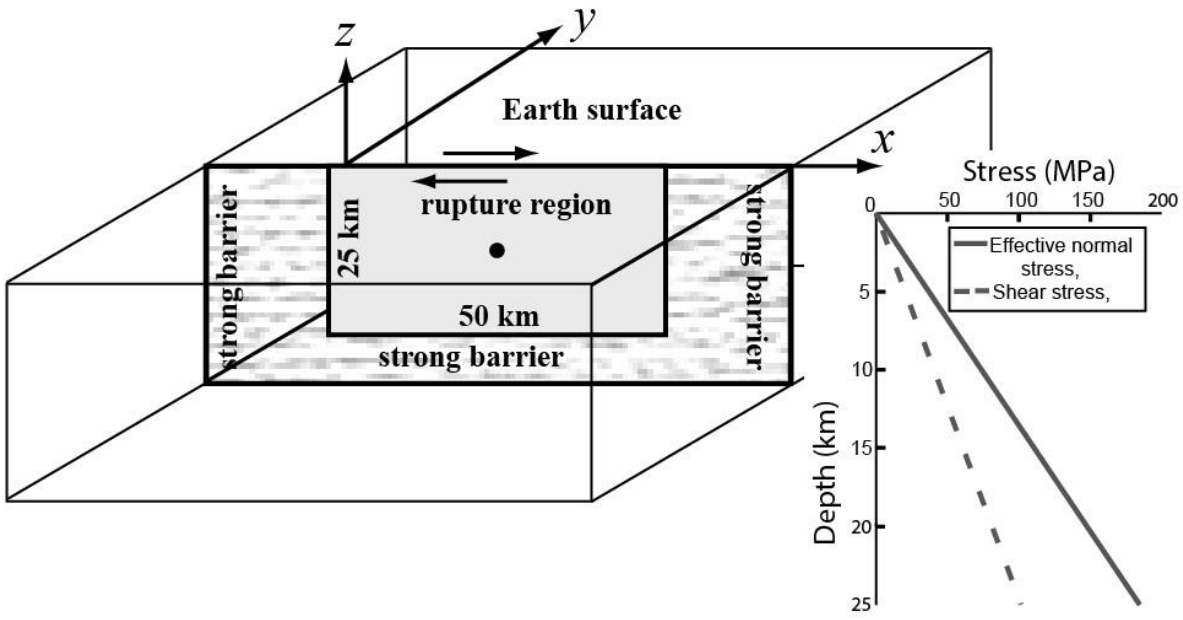

Figure S3. 3D geometry of model setup showing the stress conditions on the fault surface prior to rupture initiation. Solid black circle in the centre of the rupture region at 12 km depth is the nucleation patch.

Figure S3 and Tables S2 and S3 show model parameters and initial conditions for the representative case shown in Figure 3. We assume that the time-independent effective normal stress $\sigma = 7.4z$ (MPa), where z is in km, increases with depth. Kinematic rupture models of the Kaikoura earthquake (Cesca et al., 2017; Holden et al., 2017; Wang et al, 2018) indicate that the rupture velocity on the Kerenengu fault is subshear despite the large (>10 m) slip. To reproduce these features, the initial shear stress and fault shear strength are chosen such that the dynamic stress drop is relatively large (11 MPa at a 10-km depth) and the seismic ratio $S = (\tau_s - \tau\_xo)/(\tau\_xo - \tau_d) = 1.7$ is relatively high, discouraging the generation of supershear rupture (Dunham, 2007). We further assume the initial shear traction acts only in the horizontal direction and there is no initial vertical shear traction. For simplicity, friction parameters (μs, μd, Dc and fault cohesion) are assumed to be uniform over the fault plane.

The fault is initially at rest, and dynamic rupture is initiated by imposing a smooth, time-dependent growth of the rupture front within a 3-km nucleation patch located at 12-km depth at the centre of the fault (solid black circle in Fig. S3). The detail of the nucleation procedure is described in benchmark problem TPV22 (Harris et al., 2018, http://scecdata.usc.edu/cvws/). The rupture propagates spontaneously outside the nucleation patch. The numerical code we use is based on spectral element method (Ampuero, 2002; Kaneko et al., 2008), which has been verified through a series of community benchmark exercises (Harris et al., 2009; 2018).

To obtain the represented model shown in Figure 3, we vary seismic ratio S from 0.33 to 2.0 and the characteristic slip from 0.2 to 2.0 m and find the case that the best reproduces the observed ~15° change in rake angle of slickenlines on the Kekerengu fault and subsher

rupture propagation. If the *S* ratio is sufficiently small (e.g., the initial stress is high), supershear rupture is generated (Fig. S4), consistent with the result of Dunham (2007). In contrast, larger *S* ratio and/or *Dc* inhibit the generation of supershear rupture (Fig. S4). Although there is large variability in rake angle changes along the fault strike in a given scenario (Fig. 3), the resulting maximum or minimum instantaneous rake angle at a given location is somewhat insensitive to the input parameters (Fig. S4). Most remarkably, the sign of rake angle change with respect to the rupture direction is independent of the input parameters (Fig. S4).

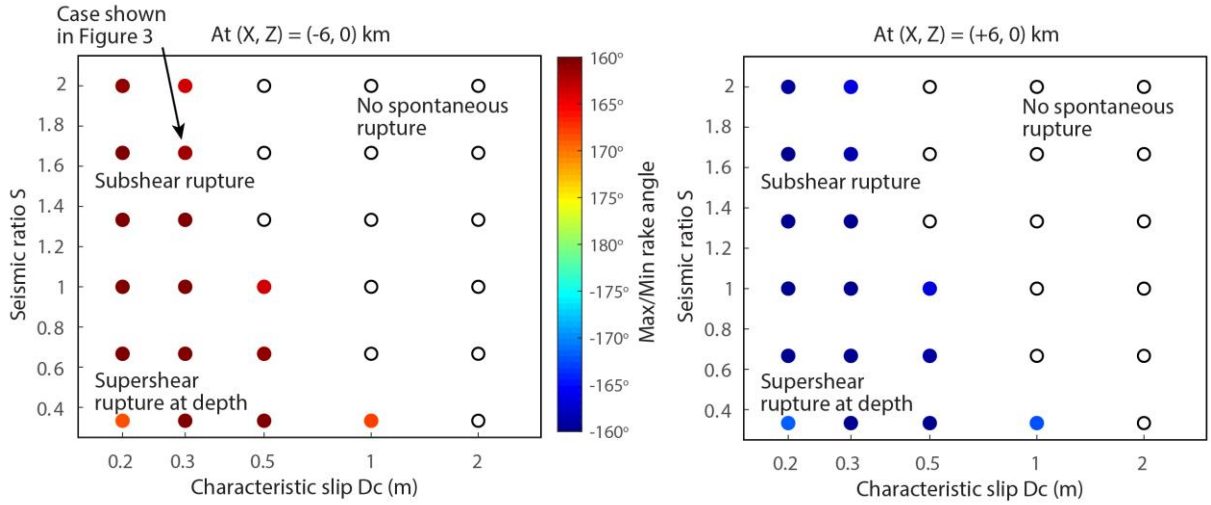

Figure S4. Variations is seismic ratio *S,* and characteristic slip distance *Dc.*

Table S2: A 1-D layered velocity model derived from the 3D velocity model of the Kaikoura earthquake source region (Eberhart-Phillips and Bannister, 2015).

Depth range (km)	Vp (km/s)	Vs (km/s)	Density (kg/m^3)
0 – 2	4.21	2.39	2300
2 – 8	4.96	2.84	2500
>8	6.00	3.46	2670

Table S3: Stress and friction parameters for the representative dynamic rupture scenario shown in Figure 3.

Parameters	Value in the representative model
Effective normal stress σ	7.34 (MPa/km)
Initial shear stress τ_xo	0.55*sigma
Initial shear stress τ_zo	0
Static friction μs	0.80

Dynamic friction μd	0.40
Characteristic slip distance Dc	0.30 m
Fault cohesion, C	2.0 MPa
Seismic ratio, S	1.7
Dynamic stress drop at 10 km depth	11 MPa

SUPPLEMENTARY MATERIAL E – SNAPSHOTS OF DYNAMIC RUPTURE

Below are a series of snapshots of our dynamic rupture model for the case shown in Figure 3 at 0.5 s intervals. The top panel shows the slip rate in m/s, the bottom panel shows the rake of instantaneous slip direction in degrees. Along anti-plane rupture boundaries (i.e., mode III), the model predicts linear slip histories. Note how at t = 2.5 s—before the rupture reaches the surface—the direction of slip immediately behind the rupture front is not 180° (horizontal), instead it is rotated by ~ 2°. Along mixed-mode rupture boundaries to the northeast of the hypocentre, it shows nearside-up slip, and to the southwest nearside-down slip. This demonstrates that the mechanism behind the rotation in slip direction is not caused by any free surface effects.

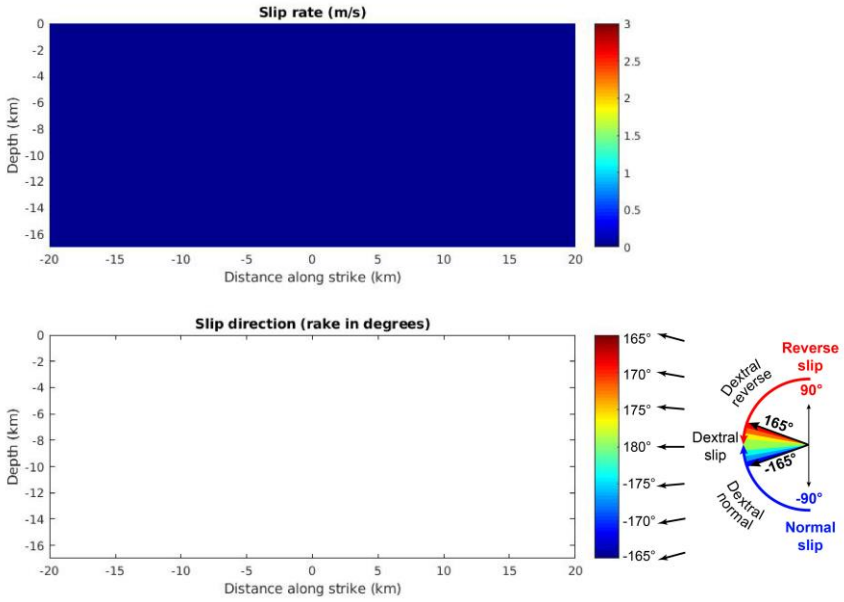

T = 0 s

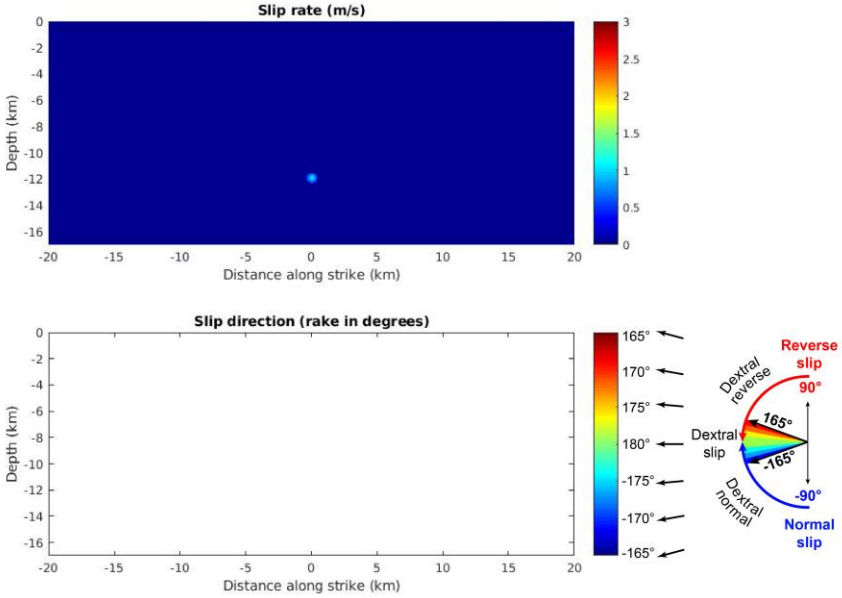
Slip rate (m/s)
Depth (km)
Distance along strike (km)
Slip direction (rake in degrees)
Depth (km)
Distance along strike (km)
Reverse slip
Dextral reverse
Dextral slip
Dextral normal
Normal slip
90°
165°
-165°
-90°

T = 0.5 s

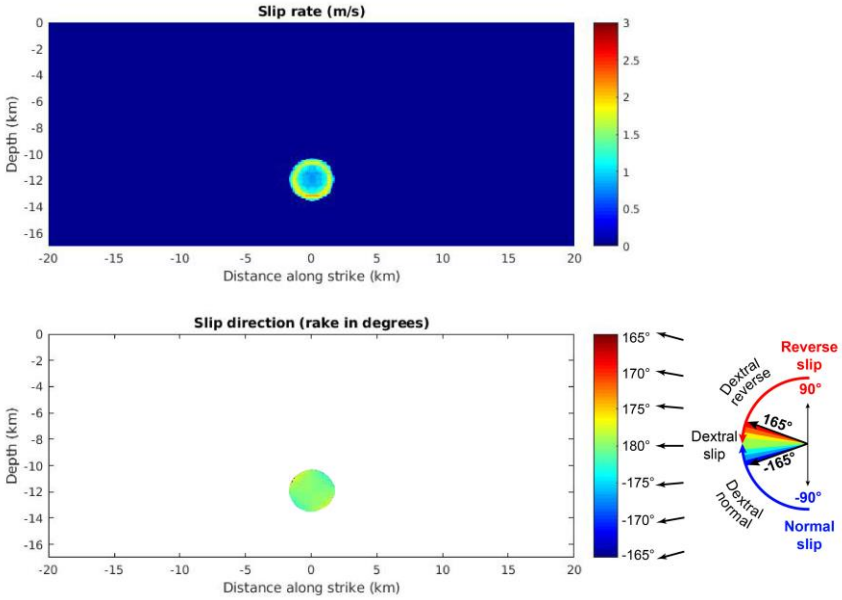
Slip rate (m/s)
Depth (km)
Distance along strike (km)
Slip direction (rake in degrees)
Depth (km)
Distance along strike (km)
Reverse slip
Dextral reverse
Dextral slip
Dextral normal
Normal slip
90°
165°
-165°
-90°

T = 1.0 s

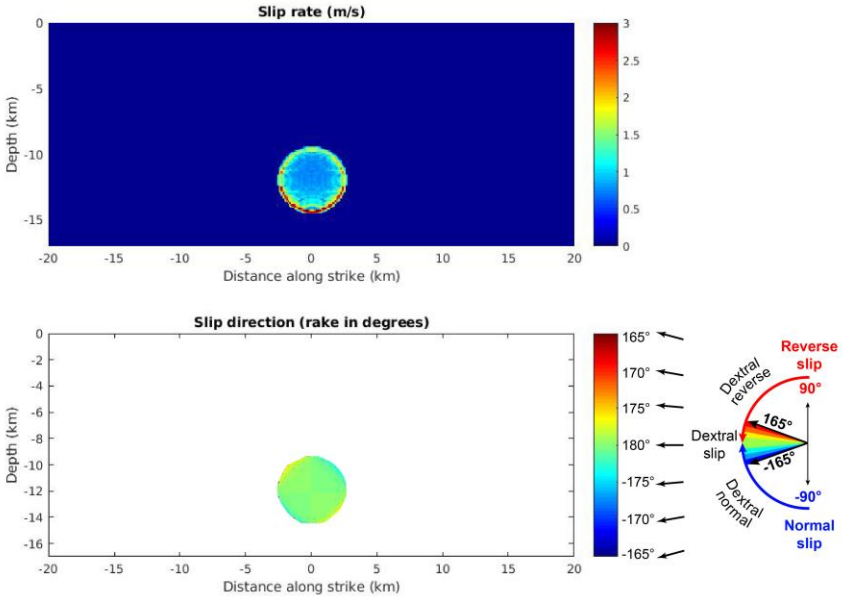
Slip rate (m/s)
Depth (km)
Distance along strike (km)
Slip direction (rake in degrees)
Depth (km)
Distance along strike (km)
Reverse slip
Dextral reverse
Dextral slip
Dextral normal
Normal slip
90°
165°
-165°
-90°

T = 1.5 s

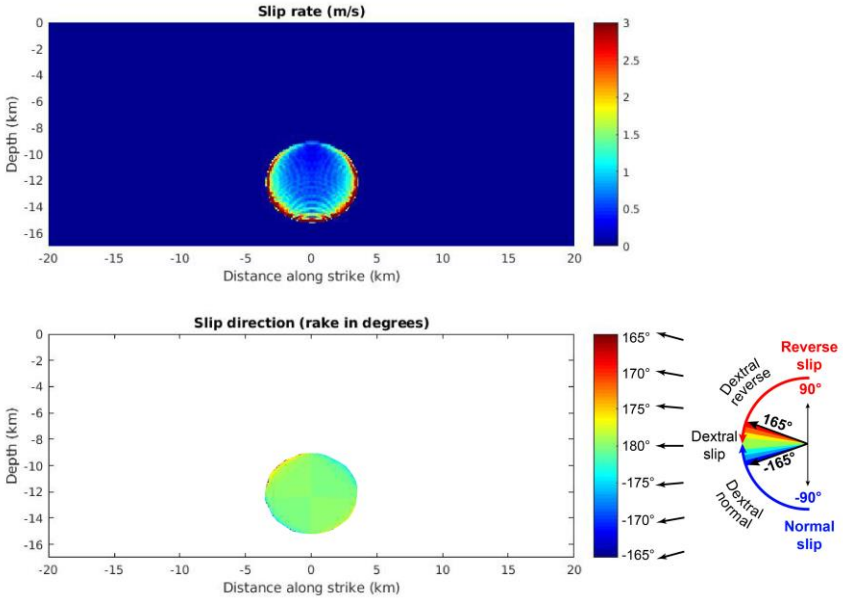
Slip rate (m/s)
Depth (km)
Distance along strike (km)
Slip direction (rake in degrees)
Depth (km)
Distance along strike (km)
Reverse slip
Dextral reverse
Dextral slip
Dextral normal
Normal slip
90°
165°
-165°
-90°

T = 2.0 s

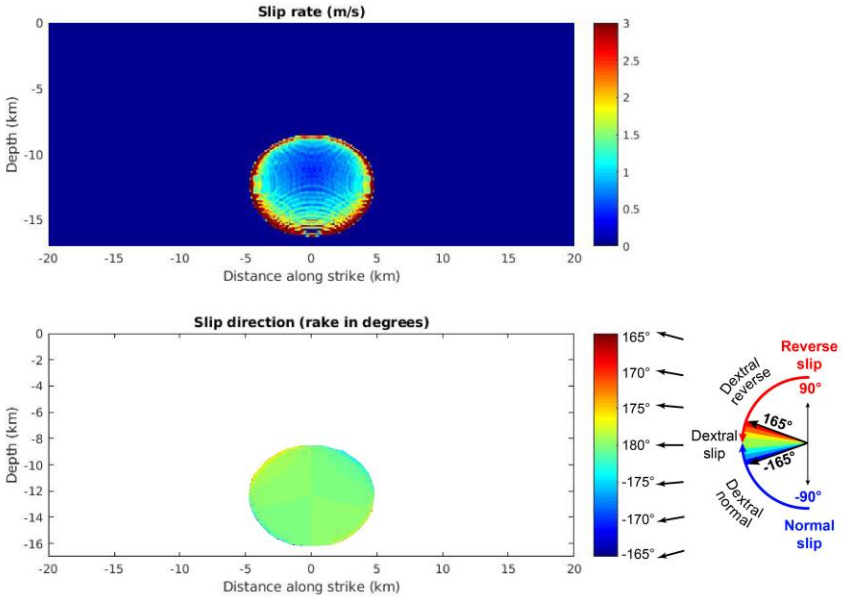
Slip rate (m/s)
Depth (km)
Distance along strike (km)
Slip direction (rake in degrees)
Depth (km)
Distance along strike (km)
Reverse slip
90°
Dextral reverse
165°
Dextral slip
-165°
-90°
Dextral normal
Normal slip

T = 2.5 s

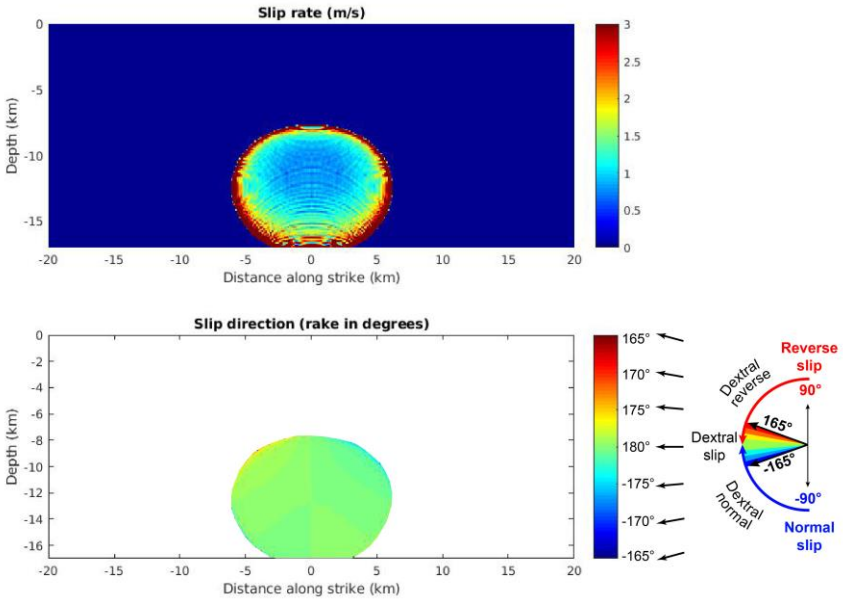
Slip rate (m/s)
Depth (km)
Distance along strike (km)
Slip direction (rake in degrees)
Depth (km)
Distance along strike (km)
Reverse slip
90°
Dextral reverse
165°
Dextral slip
-165°
-90°
Dextral normal
Normal slip

T = 3.0 s

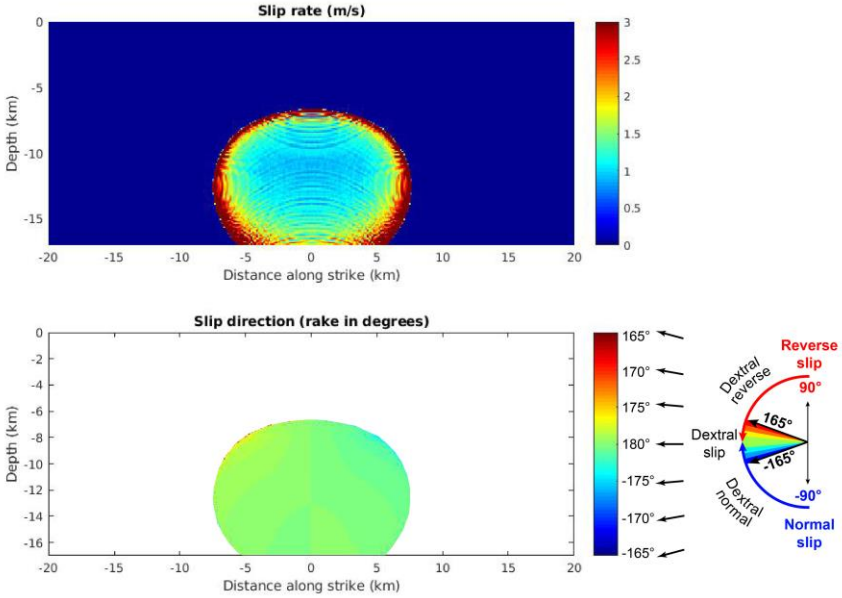
Slip rate (m/s)
Depth (km)
Distance along strike (km)
Slip direction (rake in degrees)
Depth (km)
Distance along strike (km)
Reverse slip
90°
Dextral reverse
165°
Dextral slip
-165°
-90°
Dextral normal
Normal slip

T = 3.5 s

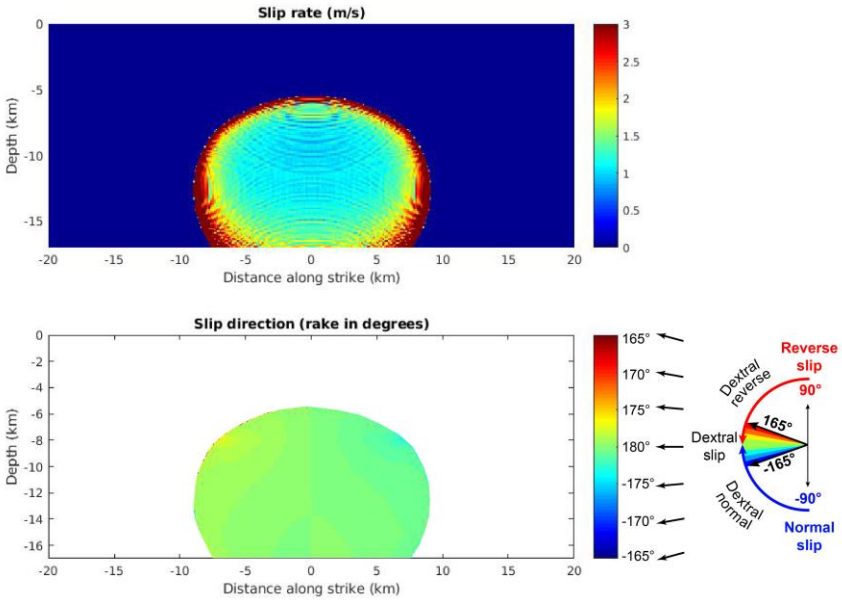
Slip rate (m/s)
Depth (km)
Distance along strike (km)
Slip direction (rake in degrees)
Depth (km)
Distance along strike (km)
Reverse slip
90°
Dextral reverse
165°
Dextral slip
-165°
-90°
Dextral normal
Normal slip

T = 4.0 s

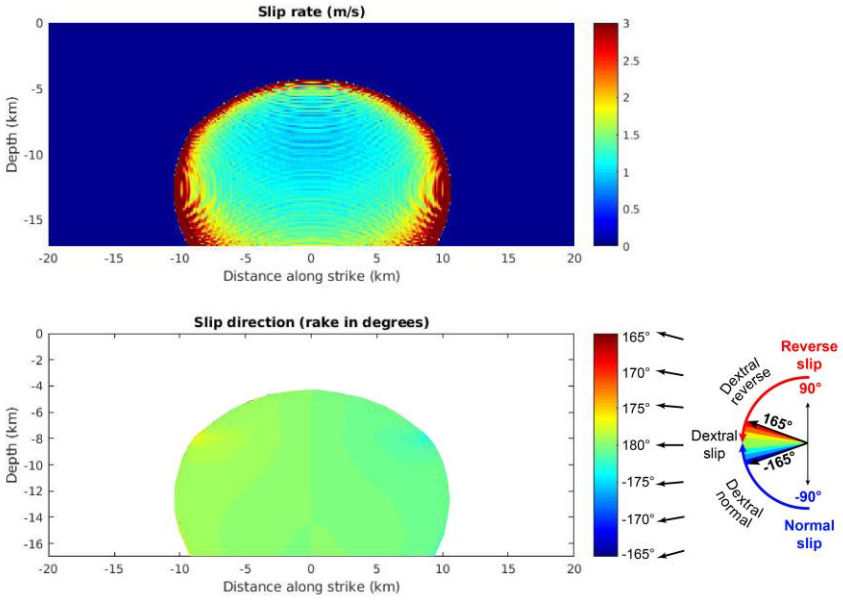
Slip rate (m/s)
Depth (km)
Distance along strike (km)
Slip direction (rake in degrees)
Depth (km)
Distance along strike (km)
Reverse slip
90°
Dextral reverse
165°
Dextral slip
-165°
Dextral normal
-90°
Normal slip

T = 4.5 s

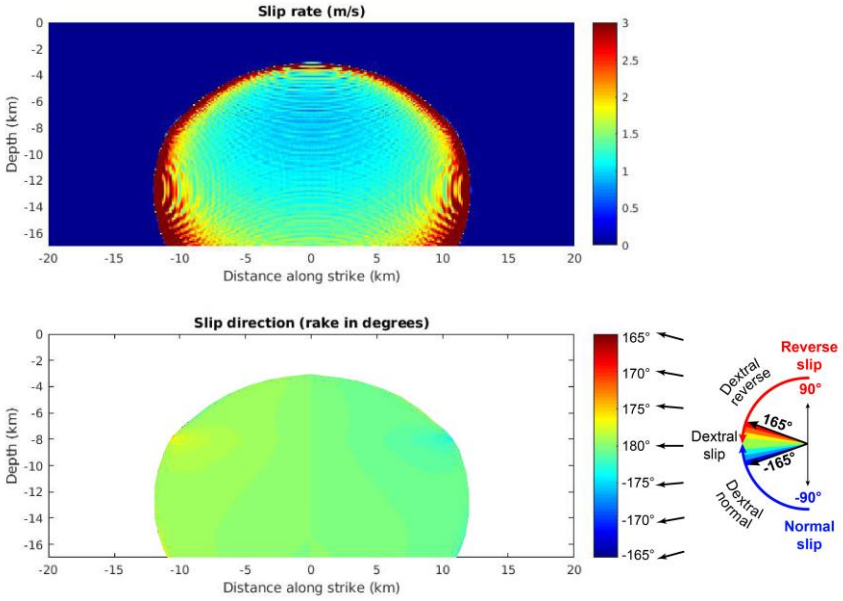
Slip rate (m/s)
Depth (km)
Distance along strike (km)
Slip direction (rake in degrees)
Depth (km)
Distance along strike (km)
Reverse slip
90°
Dextral reverse
165°
Dextral slip
-165°
Dextral normal
-90°
Normal slip

T = 5.0 s

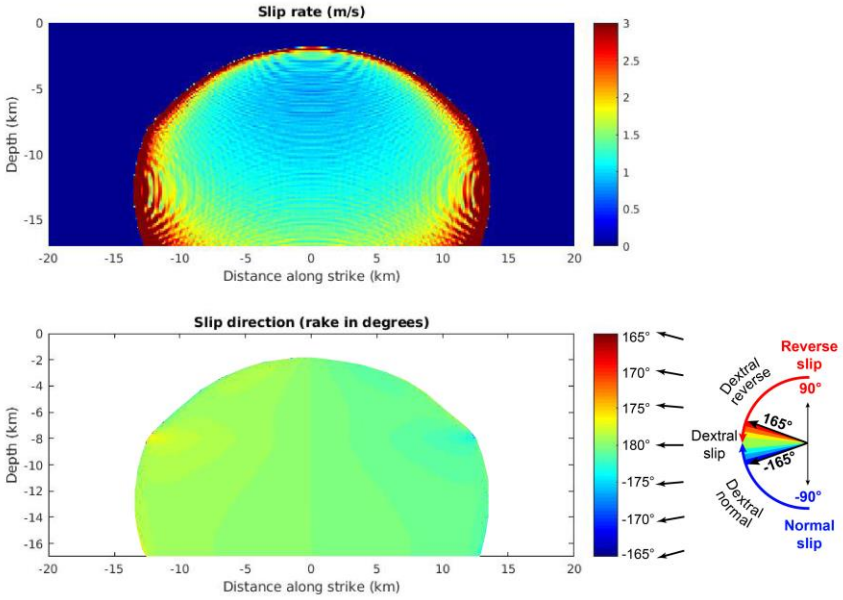
Slip rate (m/s)
Depth (km)
Distance along strike (km)
Slip direction (rake in degrees)
Depth (km)
Distance along strike (km)
Reverse slip
Dextral reverse
Dextral slip
Dextral normal
Normal slip
90°
165°
-165°
-90°

T = 5.5 s

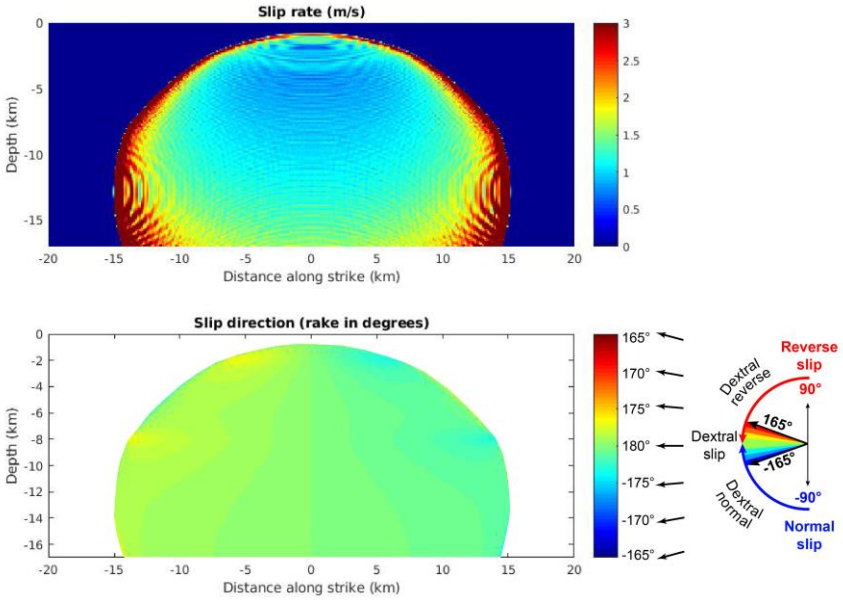
Slip rate (m/s)
Depth (km)
Distance along strike (km)
Slip direction (rake in degrees)
Depth (km)
Distance along strike (km)
Reverse slip
Dextral reverse
Dextral slip
Dextral normal
Normal slip
90°
165°
-165°
-90°

T = 6.0 s

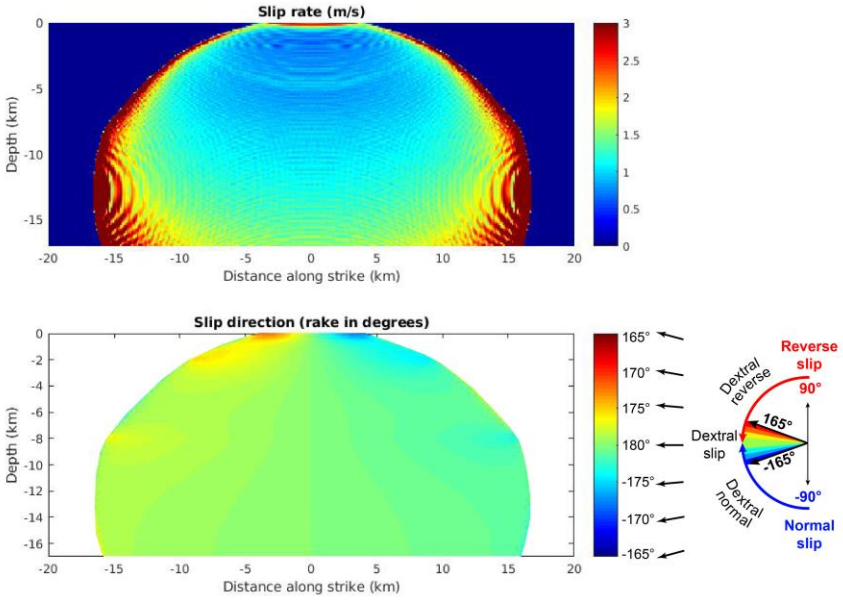
Slip rate (m/s)
Depth (km)
Distance along strike (km)
Slip direction (rake in degrees)
Depth (km)
Distance along strike (km)
Reverse slip
90°
Dextral reverse
165°
Dextral slip
-165°
Dextral normal
-90°
Normal slip

T = 6.5 s

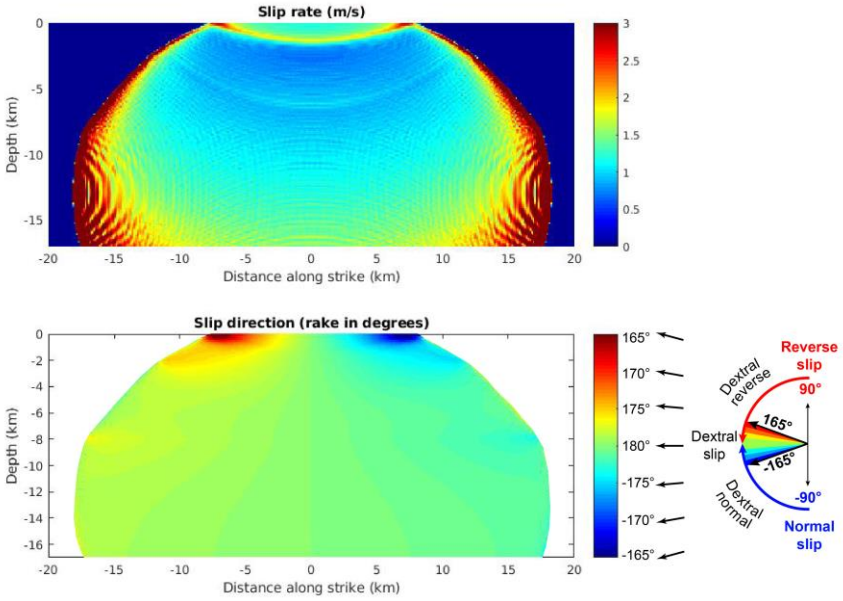
Slip rate (m/s)
Depth (km)
Distance along strike (km)
Slip direction (rake in degrees)
Depth (km)
Distance along strike (km)
Reverse slip
90°
Dextral reverse
165°
Dextral slip
-165°
Dextral normal
-90°
Normal slip

T = 7.0 s

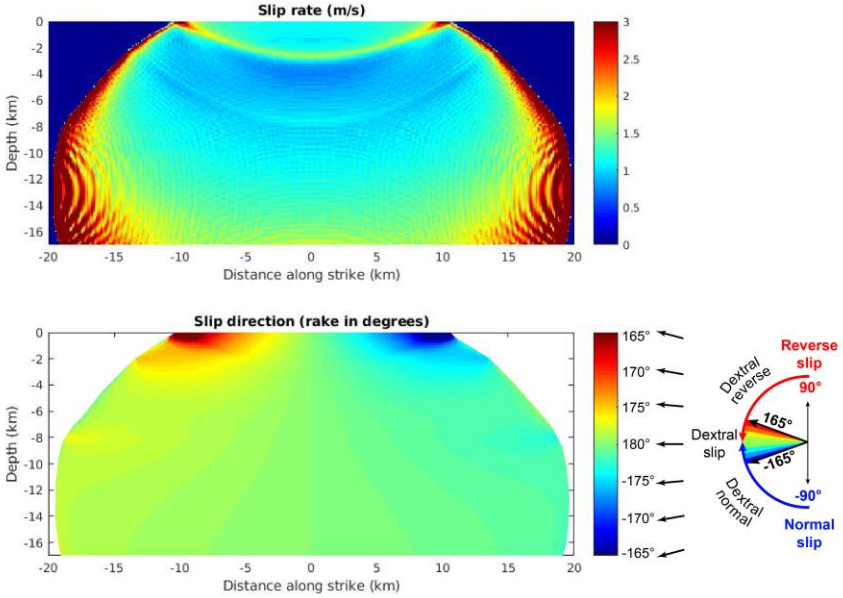
Slip rate (m/s)
Depth (km)
Distance along strike (km)
Slip direction (rake in degrees)
Depth (km)
Distance along strike (km)
Reverse slip
Dextral reverse
Dextral slip
Dextral normal
Normal slip
165°
-165°
90°
-90°

T = 7.5 s

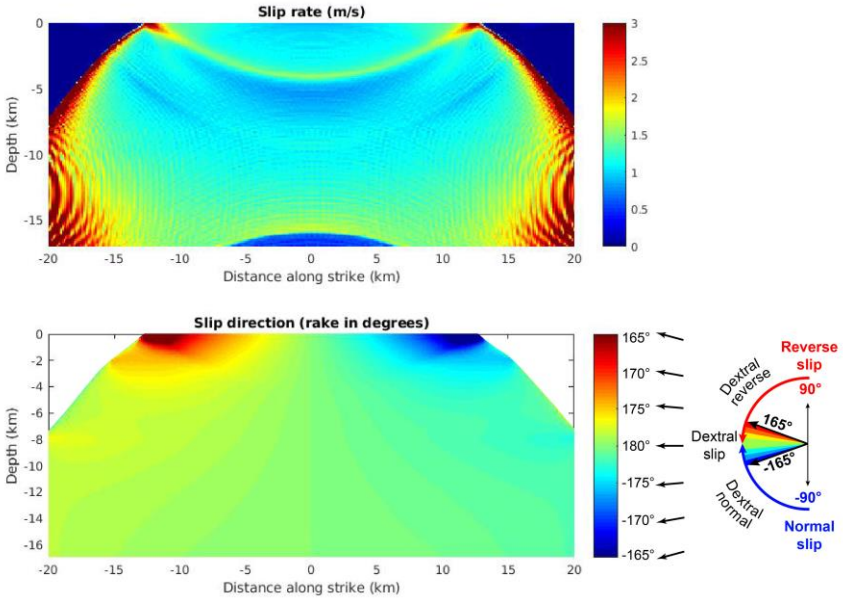
Slip rate (m/s)
Depth (km)
Distance along strike (km)
Slip direction (rake in degrees)
Depth (km)
Distance along strike (km)
Reverse slip
Dextral reverse
Dextral slip
Dextral normal
Normal slip
165°
-165°
90°
-90°

T = 8.0 s

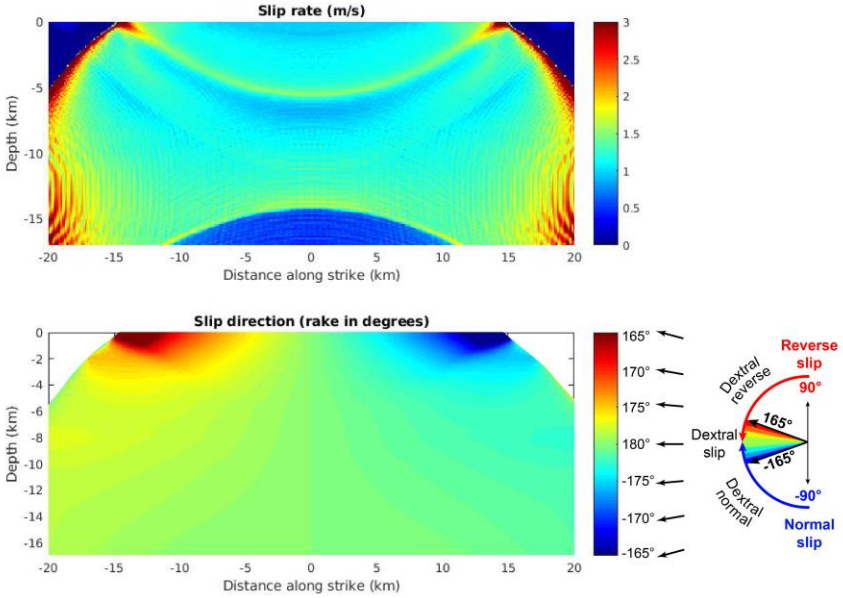
Slip rate (m/s)
Depth (km)
Distance along strike (km)
Slip direction (rake in degrees)
Depth (km)
Distance along strike (km)
Reverse slip
Dextral reverse
Dextral slip
Dextral normal
Normal slip
165°
-165°
90°
-90°

T = 8.5 s

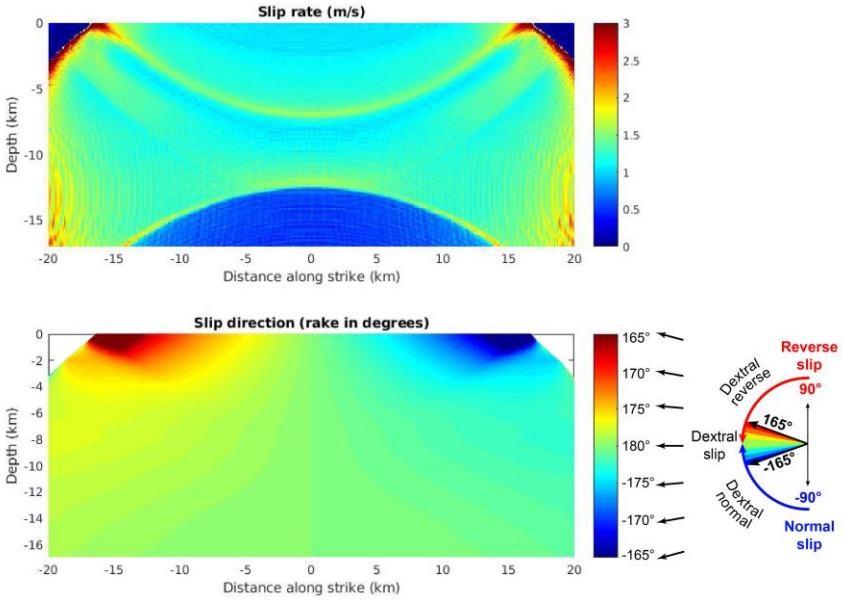
Slip rate (m/s)
Depth (km)
Distance along strike (km)
Slip direction (rake in degrees)
Depth (km)
Distance along strike (km)
Reverse slip
Dextral reverse
Dextral slip
Dextral normal
Normal slip
165°
-165°
90°
-90°

T = 9.0 s

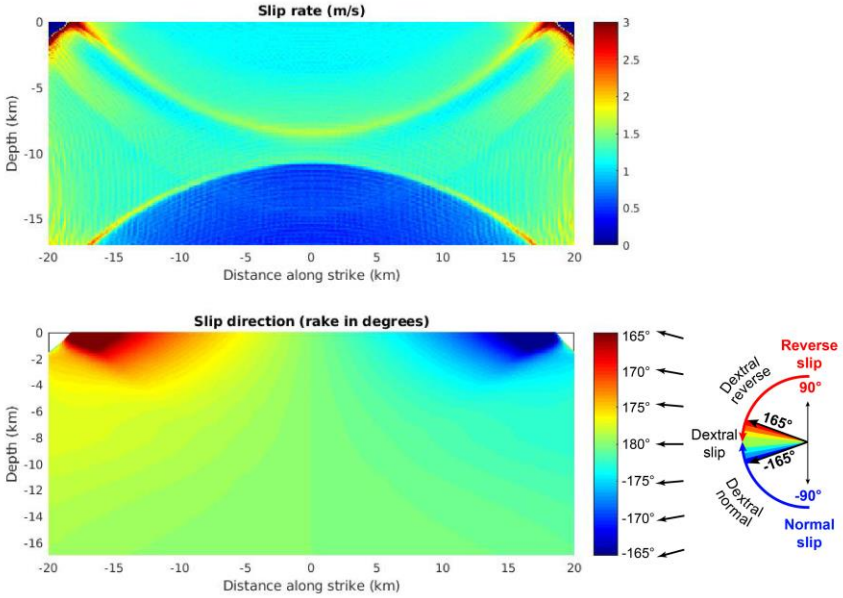
Slip rate (m/s)
Depth (km)
Distance along strike (km)
Slip direction (rake in degrees)
Depth (km)
Distance along strike (km)
Reverse slip
Dextral reverse
Dextral slip
Dextral normal
Normal slip
90°
165°
-165°
-90°

T = 9.5 s

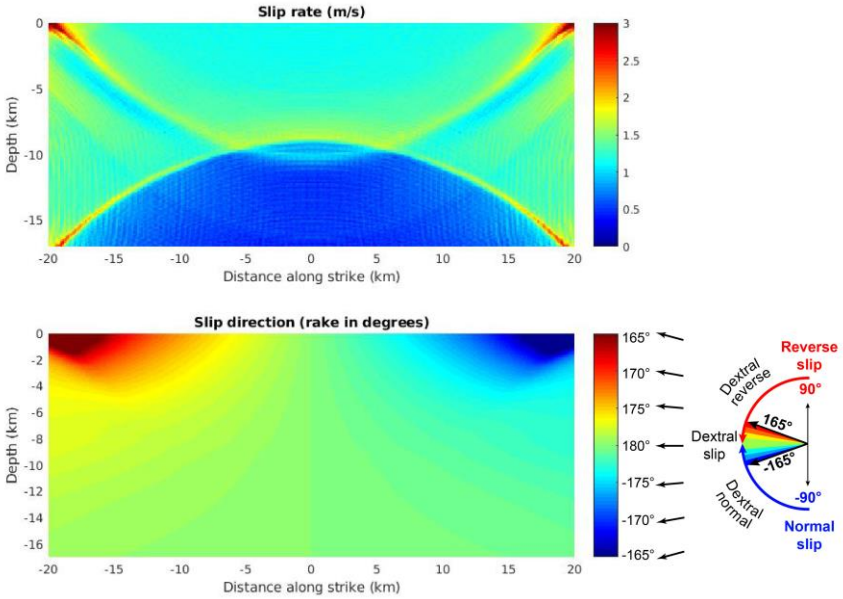
Slip rate (m/s)
Depth (km)
Distance along strike (km)
Slip direction (rake in degrees)
Depth (km)
Distance along strike (km)
Reverse slip
Dextral reverse
Dextral slip
Dextral normal
Normal slip
90°
165°
-165°
-90°

T = 10.0 s

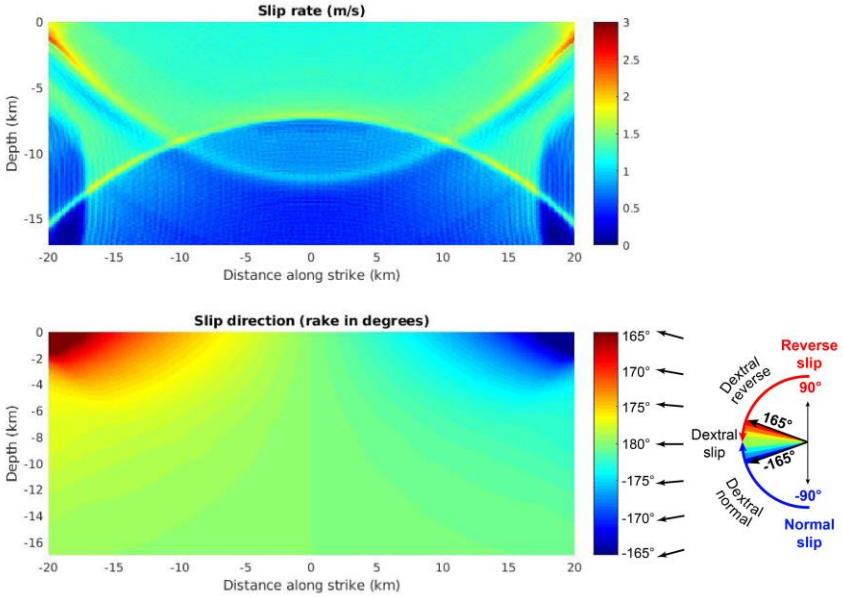
Slip rate (m/s)
Depth (km)
Distance along strike (km)
Slip direction (rake in degrees)
Depth (km)
Distance along strike (km)
Reverse slip
Dextral reverse
Dextral slip
Dextral normal
Normal slip
90°
165°
-165°
-90°

T = 10.5 s

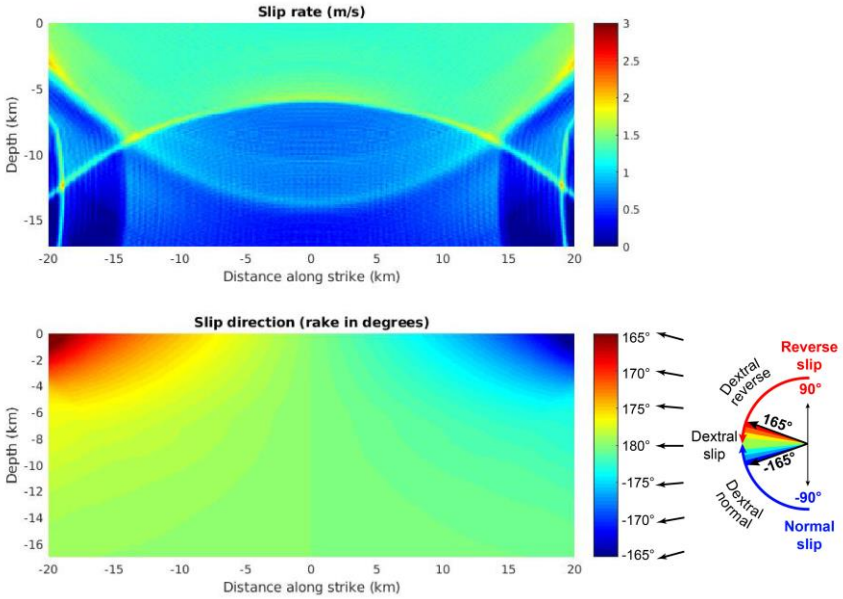
Slip rate (m/s)
Depth (km)
Distance along strike (km)
Slip direction (rake in degrees)
Depth (km)
Distance along strike (km)
Reverse slip
Dextral reverse
Dextral slip
Dextral normal
Normal slip
90°
165°
-165°
-90°

T = 11.0 s

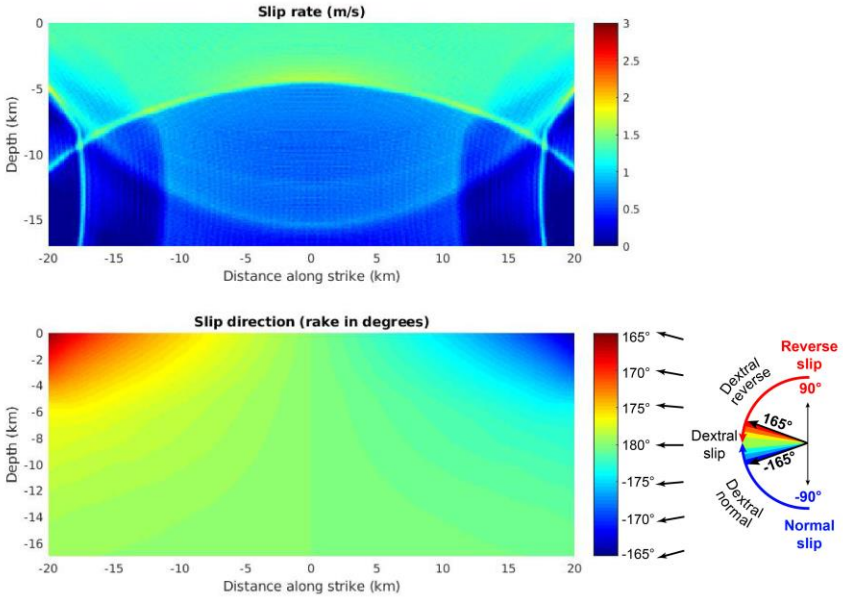
Slip rate (m/s)
Depth (km)
Distance along strike (km)
Slip direction (rake in degrees)
Depth (km)
Distance along strike (km)
Reverse slip
Dextral reverse
Dextral slip
Dextral normal
Normal slip
90°
165°
-165°
-90°

T = 11.5 s

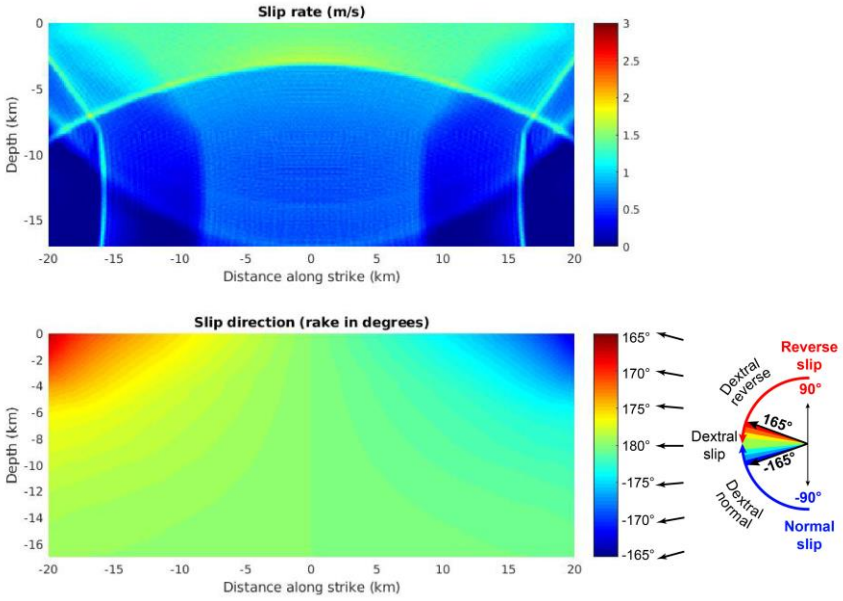
Slip rate (m/s)
Depth (km)
Distance along strike (km)
Slip direction (rake in degrees)
Depth (km)
Distance along strike (km)
Reverse slip
Dextral reverse
Dextral slip
Dextral normal
Normal slip
90°
165°
-165°
-90°

T = 12.0 s

SUPPLEMENTRAY MATERIAL F – ALTERNATIVE DYNAMIC MODELS

We consider the influence of the free surface on the mechanism of co-seismic slip direction changes. We explore this by conducting simulations where rupture propagates spontaneously across the fault surface, but does not interact with any free surface. This is achieved by nucleating the rupture at 32 km depth, while altering the pre-rupture stress profile to simulate rupture at 12 km depth. Figure S5 shows the rupture arriving at a depth of 20 km, at 7.0 s after nucleation (equivalent to 0 km, as the confining stress is set to 0 MPa at this depth). The rake angle of initial slip near the rupture tips is subdued (<5°), compared to when the free surface is present (e.g., Figure 3C in the main text), suggesting that the free surface enhances changes in rake angle.

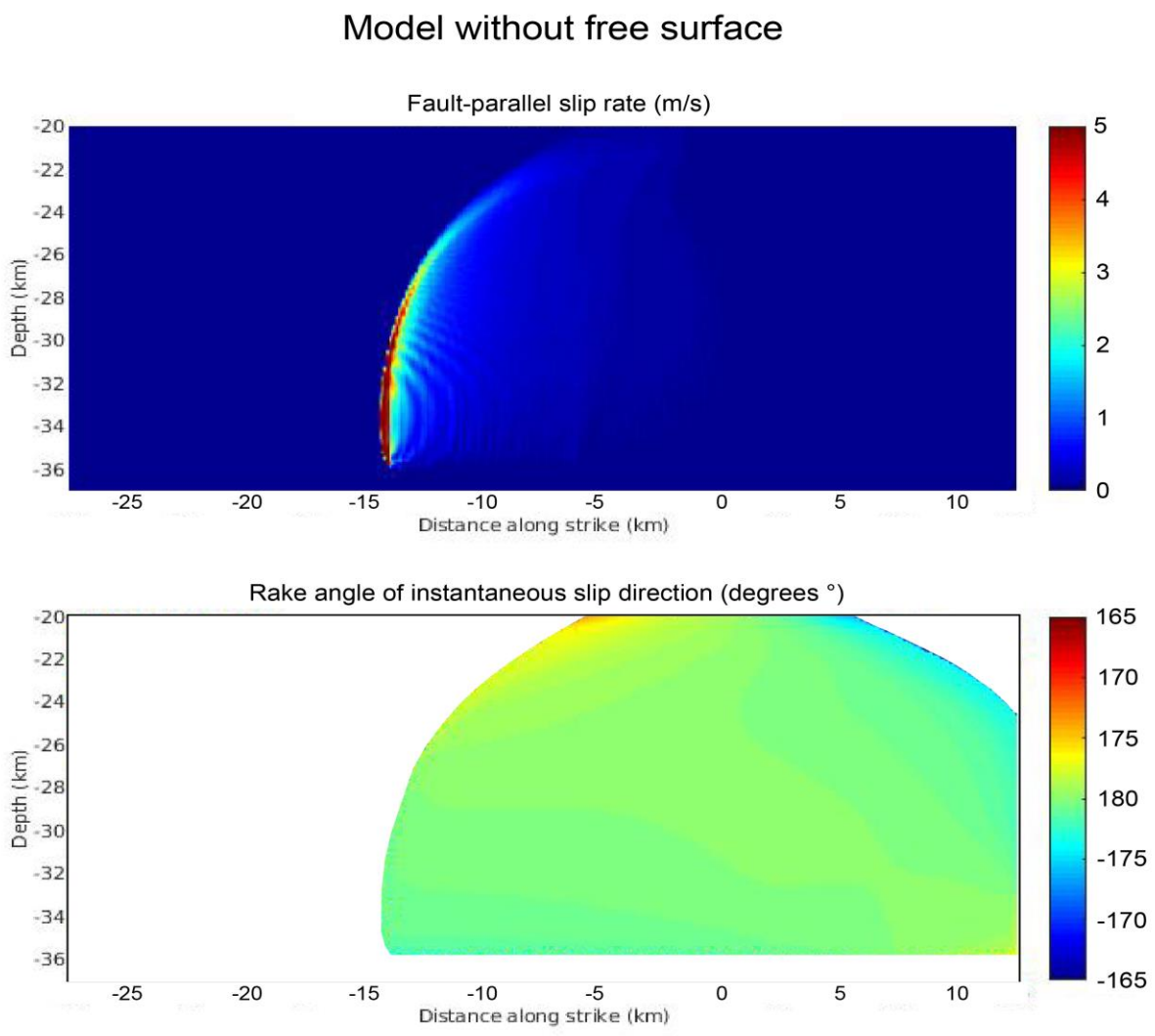

Figure S5. Snapshot of dynamic rupture at 7.0 s, with the free surface removed, showing both the slip rate (m/s) and the rake angle of instantaneous slip direction (°).

We also consider homogeneous initial stress conditions (i.e., without the depth-dependent initial stresses) on the fault surface prior to rupture nucleation (Figures S6 and S7). In this case, the ratio of dynamic stress changes, caused by slip at depth, to the absolute shear strength in the near-surface regions becomes small, suppressing the rake rotation, which is consistent with the results of Guatteri & Spudich et al. (1998).

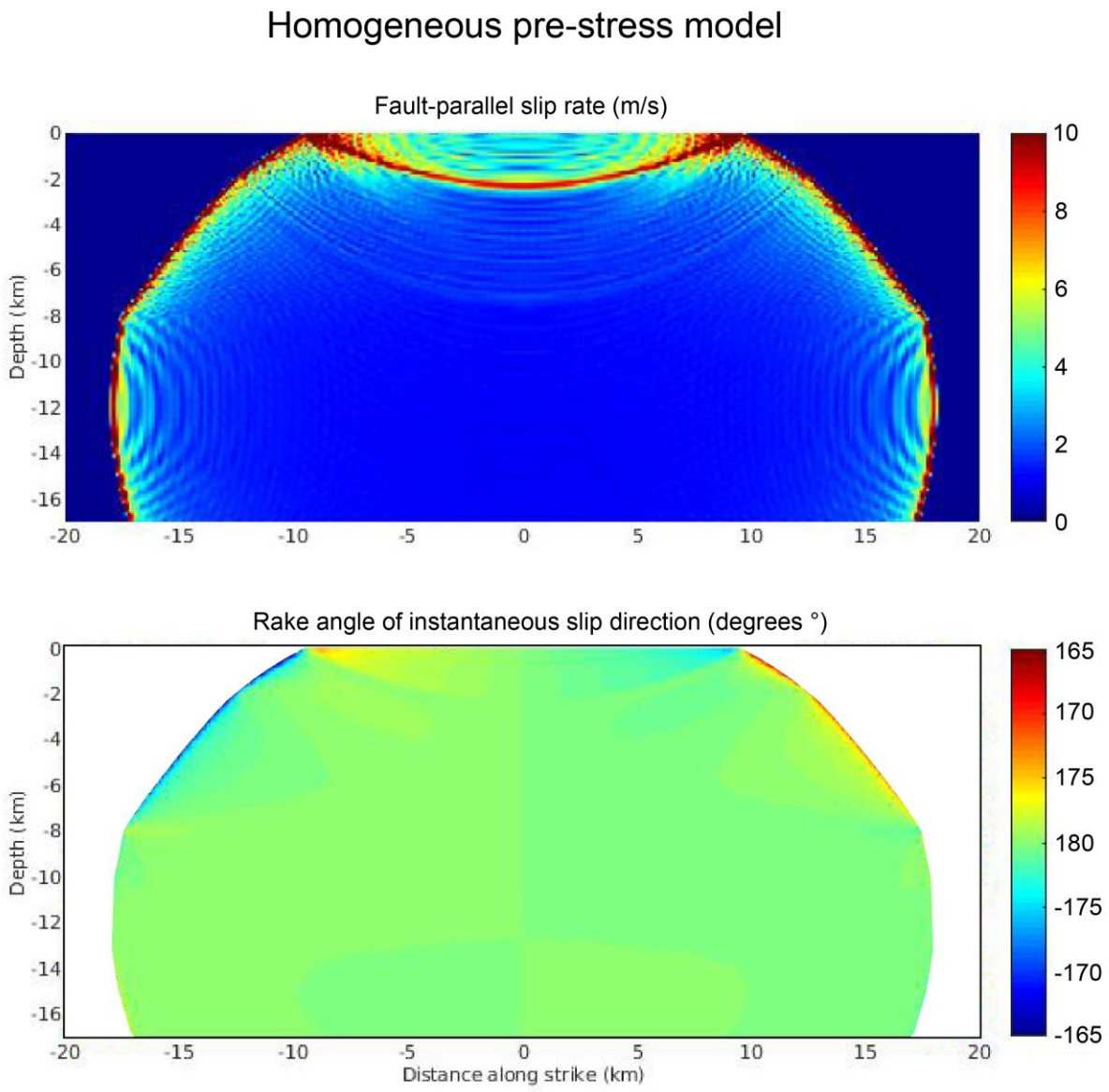

Figure S6. Snapshot of dynamic rupture at 7.0 s, with homogeneous stress, showing both the slip rate (m/s) and the rake angle of instantaneous slip direction (°).

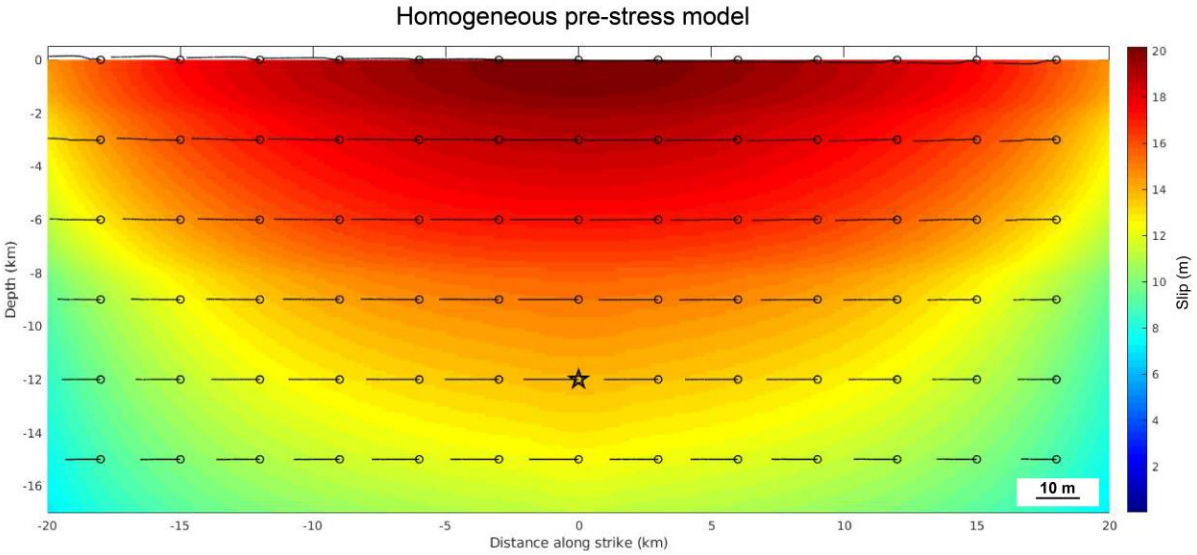

Figure S7. Final slip distribution for the model with initially homogeneous stress conditions prior to rupture nucleation. Note that changes in rake angle near the free surface are smaller than those in Figure 3.

Lastly, we consider a model to demonstrate that the convexity of the initial slip path, and its polarity with respect to the hypocentre persists even when the direction of initial shear stress is not horizontal. To do this we rotate the rake angle of initial shear stress to reflect the long-term uplift of the northwest side of the Kekerengu Fault – which was reflected in the 2016 surface slip distribution with a strike-slip to dip-slip ratio of (10:1.5) (Kearse et al., 2018). Using this ratio, we rotate the direction of pre-stress on the model fault by 8.5° (*arctan* (1.5/10)) resulting in a rake angle of 171.5°. The results of this model are summarized in Figure S8 (the figure layout is a modification to Figure 3 in the main text of this manuscript). Net uplift of the northwest side of the fault by ~1-2 m extends along the entire length of the fault, including the nodes that subside transiently on their northwest sides during the initial ~1

m of slip (e.g., Fig. S8B). Moreover, the convexity of the initial slip path at surface nodes maintains its polarity either side of the anti-plane rupture direction. For example, nodes that lie to the northeast (to the left of Fig. S8C) of the surface projection of the mode III rupture direction (e.g., Fig. S8A) show an initially convex up slip path, while nodes that lie to the southwest (to the right of Fig. S8C) of the surface projection of the mode III rupture direction (e.g., Fig. S8B) show an initially convex down slip path.

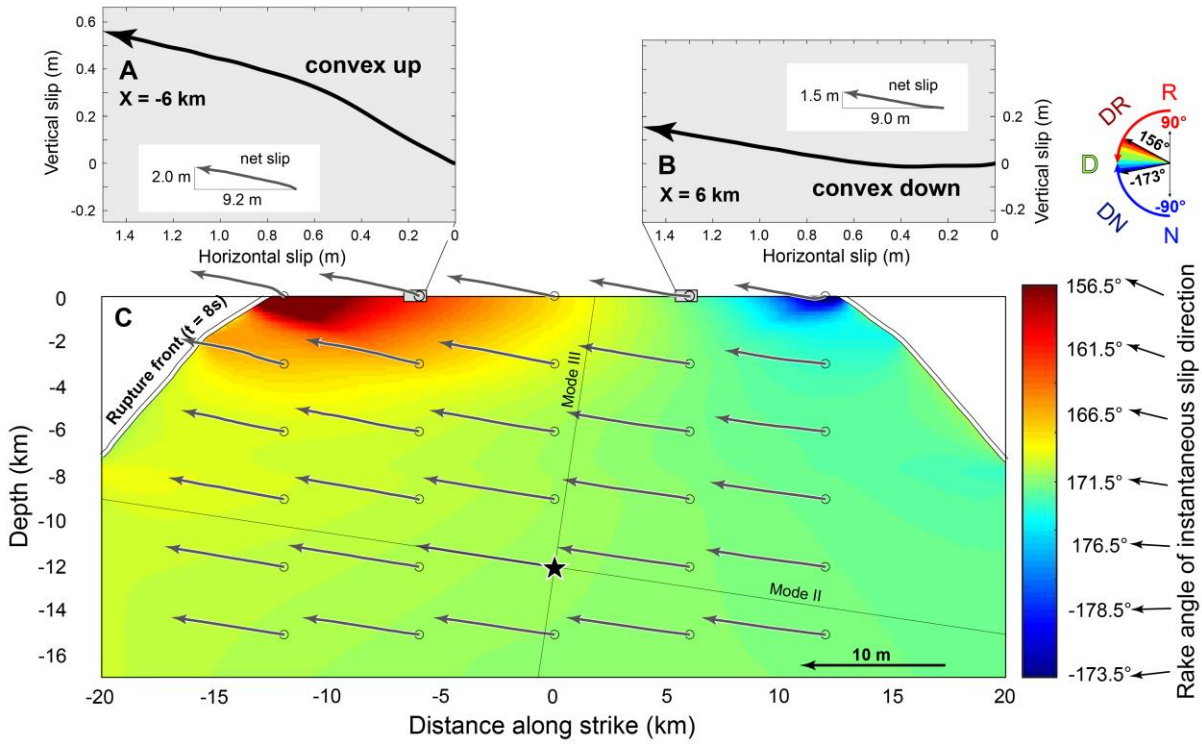

Figure S8. Fault plane view of dynamic rupture simulation results for model with reverse-dextral pre-stress (rake = 171.5°).

REFERENCES

Ampuero, J. P., Vilotte, J. P., and F. J. Sánchez-Sesma, 2002, Nucleation of rupture under slip dependent friction law: Simple models of fault zone, *J. Geophys. Res.*, 107(B12), 2324, doi: 10.1029/2001JB000452.

Arrowsmith, A., and Rhodes, D.D., 1994, Original forms and initial modifications of the Galway Lake Road scarp formed along the Emerson fault during the 28 June 1992 Landers, California, earthquake: Bulletin of the Seismological Society of America, v. 84, no. 3, p.511–527.

Avagyan, A., Ritz, J.F., Karakhanian, A. and Philip, H., 2003, Dual near-surface rupturing mechanism during the 1988 Spitak earthquake (Armenia): Izvestia of the National Academy of Sciences of the Republic of Armenia, v. 56, p.14–19.

Bizzarri, A., and Cocco, M., 2003, Slip-weakening behavior during the propagation of dynamic ruptures obeying rate-and state-dependent friction laws: Journal of Geophysical Research: Solid Earth, v. 108, no. B8.

Cesca, S., Zhang, Y., Mouslopoulou, V., Wang, R., Saul, J., Savage, M., Dahm, T., et al., 2017, Complex rupture process of the Mw 7.8, 2016, Kaikoura earthquake, New Zealand, and its aftershock sequence: Earth and Planetary Science Letters, v. 478, p. 110–120.

Crone, A.J., Machette, M.N., Bonilla, M.G., Lienkaemper, J.J., Pierce, K.L., Scott, W.E. and Bucknam, R.C., 1987, Surface faulting accompanying the Borah Peak earthquake and segmentation of the Lost River fault, central Idaho: Bulletin of the Seismological Society of America, v. 77, no. 3, p.739–770.

Crone, A.J., Machette, M.N. and Bowman, J.R., 1992, Geologic investigations of the 1988 Tennant Creek earthquakes—Implications for paleoseismicity in stable continental regions: US Geological Survey Bulletin.

Dunham, E. M., 2007, Conditions governing the occurrence of supershear ruptures under slip-weakening friction: Journal of Geophysical Research: Solid Earth, v. 112, no. B7.

Fletcher, J.M., Teran, O.J., Rockwell, T.K., Oskin, M.E., Hudnut, K.W., Mueller, K.J., Spelz, R.M., Akciz, S.O., Masana, E., Faneros, G. and Fielding, E.J., 2014, Assembly of a large

earthquake from a complex fault system: Surface rupture kinematics of the 4 April 2010 El Mayor–Cucapah (Mexico) Mw 7.2 earthquake: Geosphere, v. 10, no. 4, p.797–827.

Florensov, N.A., Solonenko, V.P., 1965, The Gobi-Altai earthquake: Acad. Nauk USSR, Moscow. English translation, US Dept. Commerce, Washington.

Guo, J., Lin, A., Sun, G., Zheng, J., 2007, Surface Ruptures Associated with the 1937 *M* 7.5 Tuosuo Lake and the 1963 *M* 7.0 Alake Lake Earthquakes and the Paleoseismicity along the Tuosuo Lake Segment of the Kunlun Fault, Northern Tibet: Bulletin of the Seismological Society of America, v. 97, no. 2, p. 474–496. doi: 10.1785/0120050103.

Haeussler, P.J., Schwartz, D.P., Dawson, T.E., Stenner, H.D., Lienkaemper, J.J., Sherrod, B., Cinti, F.R., Montone, P., Craw, P.A., Crone, A.J. and Personius, S.F., 2004, Surface rupture and slip distribution of the Denali and Totschunda faults in the 3 November 2002 M 7.9 earthquake, Alaska: Bulletin of the Seismological Society of America, v. 94, no. 6B, p.S23–S52.

Hamling, I. J., Hreinsdóttir, S., Clark, K., Elliott, J., Liang, C., Fielding, E., et al., 2017, Complex multifault rupture during the 2016 M w 7.8 Kaikōura earthquake, New Zealand: Science, v. 356, no. 6334, doi: 10.1126/science.aam7194.

Harris, R. A., Barall, M., Archuleta, R., Dunham, E., Aagaard, B., Ampuero, J. P., Day, S., et al., 2009, The SCEC/USGS dynamic earthquake rupture code verification exercise: Seismological Research Letters, v. 80, no. 1, p. 119–126.

Harris, R. A., Barall, M., Aagaard, B., Ma, S., Roten, D., Olsen, K., Ampuero, J. P., et al., 2018, A suite of exercises for verifying dynamic earthquake rupture codes: Seismological Research Letters, v. 89, no. 3, p. 1146–1162.

Holden, C., Kaneko, Y., D'Anastasio, E., Benites, R., Fry, B., and Hamling, I. J., 2017, The 2016 Kaikōura earthquake revealed by kinematic source inversion and seismic wavefield

simulations: Slow rupture propagation on a geometrically complex crustal fault network: Geophysical Research Letters, v. 44 no. 22.

Ida, Y., 1972, Cohesive force across the tip of a longitudinal-shear crack and Griffith's specific surface energy: Journal of Geophysical Research, v. 77, no. 20, p. 3796–3805.

Jones, A. E., 1915, The Pleasant Valley, Nevada, Earthquake of October 2, 1915: Bulletin of the Seismological Society of America, v. 5, p. 190–205.

Kakimi, T., Kingugasa, Y., 1977, A geologic significance of the Irozaki earthquake fault, viewed from “maturity” of faulting: Journal of the Geodetic Society of Japan, v. 22, no. 4, p.278–279.

Kaneko, Y., Lapusta, N., and Ampuero, J. P., 2008, Spectral element modeling of spontaneous earthquake rupture on rate and state faults: Effect of velocity-strengthening friction at shallow depths: Journal of Geophysical Research: Solid Earth, v. 113, no. B9, doi: 10.1029/2007JB005553.

Kaneko, Y., Fukuyama, E. and Hamling, I.J., 2017, Slip-weakening distance and energy budget inferred from near-fault ground deformation during the 2016 M_w 7. 8 Kaikōura earthquake: Geophysical Research Letters, v. 44, no. 10, p. 4765–4773.

Kearse, J., Little, T. A., Van Dissen, R. J., Barnes, P. M., Langridge, R., Mountjoy, J., et al., 2018, Onshore to offshore ground‐surface and seabed rupture of the Jordan‐Kekerengu‐Needles fault network during the 2016 Mw 7.8 Kaikōura earthquake, New Zealand: Bulletin of the Seismological Society of America, v. 108, no. 3B, p. 1573–1595, doi: 10.1785/0120170304.

Lee, J.C., Chu, H.T., Angelier, J., Chan, Y.C., Hu, J.C., Lu, C.Y. and Rau, R.J., 2002, Geometry and structure of northern surface ruptures of the 1999 Mw= 7.6 Chi-Chi Taiwan earthquake: influence from inherited fold belt structures: Journal of Structural Geology, v. 24, no. 1, p.173–192.

Lin, A., Fu, B., Guo, J., Zeng, Q., Dang, G., He, W. and Zhao, Y., 2002, Co-seismic strike-slip and rupture length produced by the 2001 Ms 8.1 Central Kunlun earthquake: Science, v. 296, no. 5575, p. 2015–2017.

Otsubo, M., Shigematsu, N., Imanishi, K., Ando, R., Takahashi, M. and Azuma, T., 2013, Temporal slip change based on curved slickenlines on fault scarps along Itozawa fault caused by 2011 Iwaki earthquake, northeast Japan: Tectonophysics, v. 608, p. 970-979, doi: 10.1016/j.tecto.2013.07.022.

Otsuki, K., Minagawa, J., Aono, M., and Ohtake, M., 1997, On the curved striations of Nojima seismic fault engraved at the 1995 Hyogoken-Nambu earthquake, Japan: Journal of the Seismological Society of Japan, v. 49, p. 451–460.

Palmer, A. C., & Rice, J. R., 1973, The growth of slip surfaces in the progressive failure of over-consolidated clay: Proceedings of the Royal Society of London. A. Mathematical and Physical Sciences, v. 332, no. 1591, p. 527–548.

Pan, J., Li, H., Si, J., Pei, J., Fu, X., Chevalier, M.L. and Liu, D., 2014, Rupture process of the Wenchuan earthquake (Mw 7.9) from surface ruptures and fault striations characteristics: Tectonophysics, v. 619, p.13–28.

Philip, H. and Megard, F., 1977, Structural analysis of the superficial deformation of the 1969 Pariahuanca earthquakes (central Peru): Tectonophysics, v. 38, no. 3–4, p.259-278.

Philip, H. and Meghraoui, M., 1983, Structural analysis and interpretation of the surface deformations of the El Asnam earthquake of October 10, 1980: Tectonics, v. 2, no. 1, p.17–49.

Shimamoto, T., 1996, Surface faults and damage associated with the 1995 Neftegorsk earthquake: Journal of the Geological Society of Japan, v. 102, p.894–907.

Slemmons, D.B., 1957, Geological effects of the Dixie valley-Fairview peak, Nevada, earthquakes of December 16, 1954: Bulletin of the Seismological Society of America, v. 47, no. 4, p. 353–375.

Treiman, J.A., Kendrick, K.J., Bryant, W.A., Rockwell, T.K. and McGill, S.F., 2002, Primary surface rupture associated with the M w 7.1 16 October 1999 Hector Mine earthquake, San Bernardino county, California: Bulletin of the Seismological Society of America, v. 92, no. 4, p.1171–1191.

Wang, T., Wei, S., Shi, X., Qiu, Q., Li, L., Peng, D., Barbot, S., et al., 2018, The 2016 Kaikōura earthquake: Simultaneous rupture of the subduction interface and overlying faults: Earth and Planetary Science Letters, v. 482, p. 44–51.

Witkind, I.J., Myers, W.B., Hadley, J.B., Hamilton, W. and Fraser, G.D., 1962, Geologic features of the earthquake at Hebgen Lake, Montana, August 17, 1959: Bulletin of the Seismological Society of America, v. 52, no. 2, p.163–180.

Xu, W., Feng, G., Meng, L., Zhang, A., Ampuero, J. P., Bürgmann, R., and Fang, L., 2018, Transpressional rupture cascade of the 2016 Mw 7.8 Kaikoura earthquake, New Zealand: Journal of Geophysical Research: Solid Earth, v. 123, no. 3, p. 2396–2409.